NOVEL METHODS IN MESO-SCALE AND NANO-SCALE ACTUATION

A Dissertation

Presented to the Faculty of the Graduate School

of Cornell University

In Partial Fulfillment of the Requirements for the Degree of

Doctor of Philosophy

by

Erick John Ball

August 2016

NOVEL METHODS IN MESO-SCALE AND NANO-SCALE ACTUATION

Erick Ball, Ph. D.

Cornell University 2016

Mechanical systems at all length scales depend on actuators to drive their motion, so advancements in actuation technology can dramatically expand their utility. Two radically different machine environments are addressed here. In each of them, previously untried concepts for actuation mechanisms show the potential to reduce size and weight while opening up new application spaces.

At the meso-scale, fluidic artificial muscles have been studied as a lightweight and economical way to generate high forces and biomimetic responses in prosthetics, assistive devices, and small-scale robotics. A new geometric mechanism for converting fluid flow into muscle contraction is demonstrated: the knitted-sleeve artificial muscle. Analysis shows that a knitted sleeve offers greater contraction range and a more constant force output than previous artificial muscle geometries. It also more closely matches the properties of biological muscle. Techniques for numerical modeling of sleeve and bladder geometries are shown to improve prediction accuracy and illuminate ways to optimize artificial muscles for different applications.

At the nano-scale, new composite multiferroic materials have opened up possibilities for electrical control of ferromagnetic structures, including the piezoelectric rotation of

magnetization in nano-rings. A method is proposed for generating torque in a multiferroic motor by coupling the magnetic field of a nano-ring to a bar magnet in the center of the ring. Strain applied to the ring causes a misalignment between the bar and the magnetization of the ring, and should cause the bar to rotate. Analysis shows that the potential torque density of multiferroic actuators is higher than that of electrostatic actuators.

BIOGRAPHICAL SKETCH

Erick Ball grew up in Woodinville, WA and attended the U.S. Air Force Academy before graduating from Swarthmore College. There he studied engineering with a minor in physics, and spent a summer evaluating the feasibility of comet interception at the Center for Space Nuclear Research in Idaho. Later, he spent a semester working on renewable energy integration at NASA's Glenn Research Center. He came to Cornell in 2011 and joined the Laboratory for Intelligent Machine Systems, receiving an M.S. in Mechanical Engineering in 2014. He now works at Energy Research, Inc. in Maryland.

In memory of my brother, Ben, who would have done something breathtaking.

ACKNOWLEDGMENTS

I would like to thank my advisor, Ephrahim Garcia, who taught me to think outside the boxes that limit engineering; Augusta Christensen, who has been the light of my life for seven years; my parents, who showed me what curiosity can mean; Greg Carman; Mike Meller; Mark Nowakowski; Hyunmin Sohn; and my committee, for helping me see this through to the end. I also thank the Center for Translational Applications of Nanoscale Multiferroic Systems, for funding support.

TABLE OF CONTENTS

LIST OF FIGURES

LIST OF TABLES

PREFACE

This dissertation addresses the topic of actuator development with three chapters in two very different domains, and each with different goals and methods. What they share is analytical and computational evaluation of the dependence of actuator forces on device geometry, and how this dependence gives rise to equilibrium conditions that constrain its motion.

Chapters 1 and 2 are in the domain of pneumatically actuated artificial muscles, a class of meso-scale (millimeters to centimeters) actuation technologies that have applications including robotics research, factory automation, and medical prosthetics. Chapter 1 presents a novel design, the knitted-sleeve artificial muscle, that improves on certain limitations of these actuators in hopes of expanding the space of applications where they may be useful. Chapter 2 focuses on streamlining the design process for the popular McKibben artificial muscle, by using computational techniques to improve modeling accuracy, especially with regard to the elastic bladder component. This can allow the design of an artificial muscle to meet specific force and stroke requirements with reduced need for prototyping. The analysis techniques are applicable to certain other artificial designs, including the knitted-sleeve muscle. Chapter 3 is concerned with dynamic analysis of nanoscale magnetic systems, as a preliminary step toward development of a multiferroic motor. The approach it takes is primarily theoretical, with the intent to illuminate the feasibility and operating characteristics of spinning motion driven by magnetoelectrically generated fields.

CHAPTER 1

MODELING AND TESTING OF A KNITTED-SLEEVE FLUIDIC ARTIFICIAL MUSCLE

Abstract

The knitted-sleeve fluidic muscle is similar in design to a traditional McKibben muscle, with a separate bladder and sleeve. However, in place of a braided sleeve, it uses a tubular-knit sleeve made from a thin strand of flexible but inextensible yarn. When the bladder is pressurized, the sleeve expands by letting the loops of fiber slide past each other, changing the dimensions of the rectangular cells in the stitch pattern. Ideally, the internal volume of the sleeve would reach a maximum when its length has contracted by 2/3 from its maximum length, and although this is not reachable in practice, preliminary tests show that free contraction greater than 50% is achievable. The motion relies on using a fiber with a low coefficient of friction in order to reduce hysteresis to an acceptable level. In addition to increased stroke length, potential advantages of this technique include slower force drop-off during the stroke, more useable energy in certain applications, and greater similarity to the force-length relationship of skeletal muscle. Its main limitation is its potentially greater effect from friction compared to other fluidic muscle designs.

1.1 Introduction

Artificial muscle actuators have existed since the 1950s and are used in robotics, biomimetic systems, medical devices, and aerospace systems [1,2,3]. Artificial muscles are defined by their similarity to biological muscles in shape and motion—they are tensile actuators, usually with little or no ability to apply compressive force, and as a result they may

be constructed from soft and/or lightweight materials. Among the fluidic artificial muscles (those controlled by the application of pressurized gas or liquid) force-to-weight and power-to-weight ratios can be quite high, but their range of motion is typically limited to 40% or less of their extended length [4]; this compares unfavorably with pneumatic cylinders which have maximum contraction limited to 50% for most designs and higher for telescoping cylinders [5].

The most common type of fluidic muscle, the McKibben muscle, is easy to manufacture but rarely contracts more than 35% [6]; this limitation requires axial space to be allocated for the actuator that is approximately three times the require ranged of motion, which can be cumbersome and limit the usefulness of the device. Because fluidic muscles generally create only tension forces, they are often used in antagonistic pairs to provide motion in both directions, increasing the volume they occupy. The knitted-sleeve fluidic muscle (Figure 1.1) is a more flexible alternative to the McKibben muscle that could be used in its place in many applications, and is manufactured and operated in an almost identical simple and cheap manner. Instead of the braided sleeve of a McKibben muscle, consisting of a mesh of helical threads, it uses a knitted sleeve in which the thread forms a series of rectangular stitches. Abel, Luntz, and Brei [7] give an excellent description of the basic types of knitting and some of their potential uses in actuation. The bladder, pressure fittings, and end attachments of a knitted muscle are the same as those of McKibben muscles.

This paper summarizes previous related work, including several varieties of fluidic artificial muscles, and then develops a simple model for the knitted muscle quasi-static force curve, along with more complex models to improve accuracy. It describes the results of

preliminary tensile testing on a prototype knitted muscle, and discusses the ramifications of this new artificial muscle.

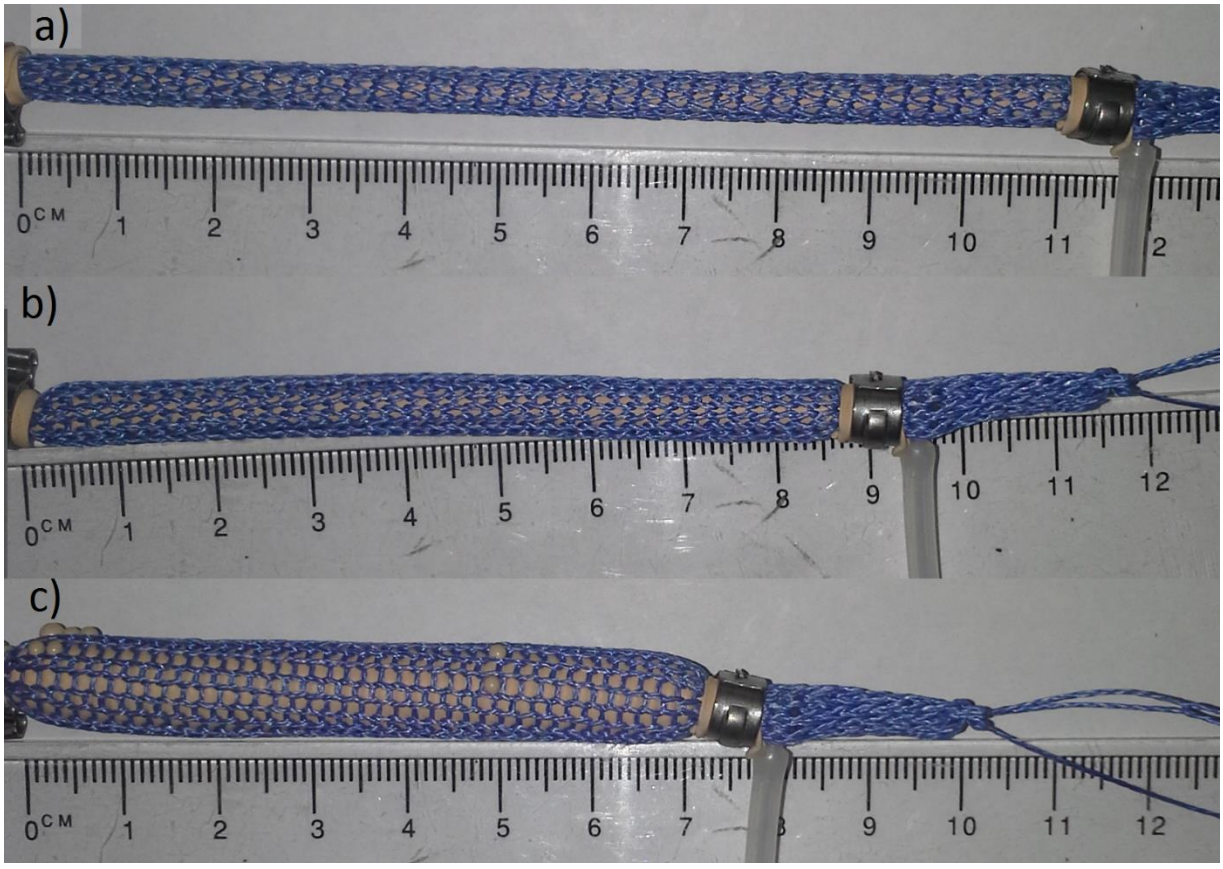

Figure 1.1: A knitted-sleeve fluidic artificial muscle with eight stitches per row of Spectra thread: a) fully stretched; b) in its relaxed state; c) pressurized with air at the highest pressure tolerable by the thin bladder, approximately 200 kPa.

1.2 Background and Previous Work

The McKibben muscle, invented in the 1950s, was the earliest practical air muscle and remains popular [1]. It uses a tubular bladder (often rubber) with a pressure inlet at one end, enclosed in a braided (bias-woven) fiber sleeve [8,9,1]. Each fiber winds in a helical path

around the bladder. The bladder and sleeve are clamped together at the ends. When the bladder is pressurized it presses outward on the sleeve and causes it to expand radially, increasing the fiber angle and decreasing the length of the muscle as the internal volume increases (Figure 1.2). An ideal McKibben muscle with an initial braid angle of zero can contract theoretically up to 42%, at which point the volume contained inside the shell reaches a maximum; further contraction would reduce the volume of pressurized fluid it holds [6,1,10,11]. In practice, initial braid angle is limited by the space taken up by the bladder and sleeve, and they can often contract by about 30% [6,10,11]. The motion is generally similar to that of a biological muscle on the ascending limb portion of its motion range [12]. Variations of this design include combining the bladder and sleeve by rubberizing the sleeve, and leaving the bladder ends disconnected from the sleeve [13, 14]. Various end fittings have been devised to transmit tensile force from the sleeve fibers into the mounting points. Several versions of McKibben muscles are available commercially from companies including Festo and the Shadow Robot Company.

Figure 1.2: McKibben muscle actuation: a) unpressurized muscle at its relaxed length; b) the pressurized (approximately 500 kPa) muscle expands in diameter but contracts in length.

Pleated pneumatic artificial muscles [4] use a bladder material with high stiffness and tensile strength, with no braided sleeve, and numerous axial folds so that it has a pleated tube shape when stretched, but when inflated it takes on an approximately spherical shape. The maximum theoretical contraction is 54%, and the practical maximum is 45%. For a given stroke length, the pleated muscle occupies less axial stroke length than a McKibben muscle, but requires more radial space because of its inflated shape.

The Paynter knitted muscle works on the same basic principle as the pleated pneumatic artificial muscle, but is designed with a separate bladder and sleeve, each having tubular ends and a roughly spherical expanded section at the center [4,15]. The bladder is an elastomer and the sleeve is made by knitting a stiff fiber like Dacron or Kevlar in a tubular pattern, with looser stitches in the middle to make the expanded section. The bladder is placed inside the sleeve and pressurized to fully expand until stopped by the sleeve, then the bladder

and sleeve are bonded together with an adhesive. Note that this adhesive bonding prevents any sliding of the fiber strand crossings in the sleeve, preserving the wide, square-shaped stitches near the center and tight stitches near the ends. Pleats form irregularly when the actuator is stretched, but can be improved by heating within a pleated mold.

1.3 Quasi-Static Modeling

1.3.1 Traditional McKibben Muscle Model

The ideal model of a McKibben muscle, called the Gaylord force model, is based on the sleeve geometry and assumes a conservative system in which fluid is supplied externally at a constant pressure [1]. Tensile force F is taken to be the derivative of potential energy U with respect to actuator length L. All contributions to energy are neglected except that of the pressurized fluid source, which depends only on gauge pressure P and muscle volume V:

$$F = \frac{dU}{dL} = -P\frac{dV}{dL} \tag{1.1}$$

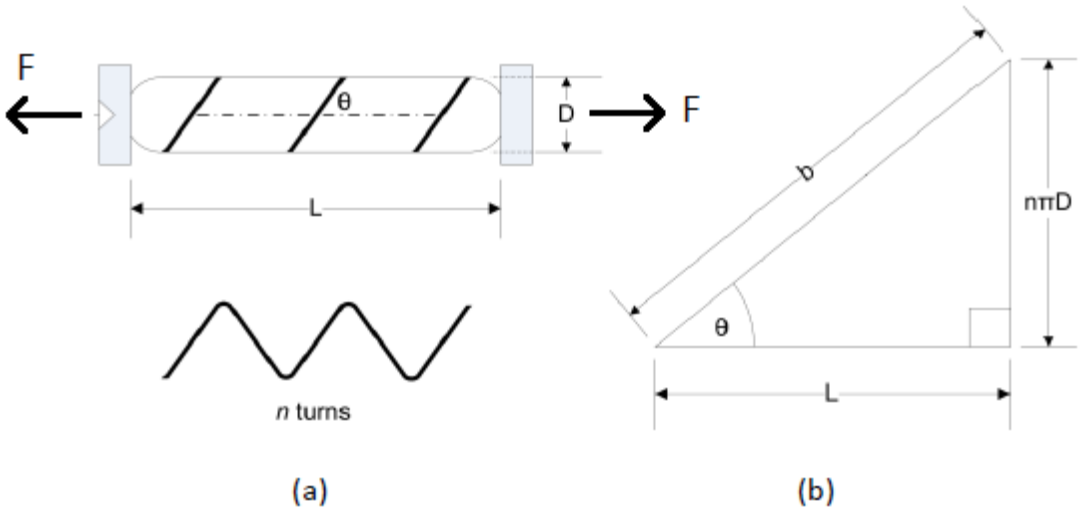

Figure 1.3: Shell geometry: a) helically wound strand forming part of the shell cylinder; b) unwound strand showing how the dimensions are related geometrically. Adapted from Tiwari and Meller [11].

The geometric constraint of the helical strands controls the relationship between length and circumference, which in turn determine the volume. Each strand (Figure 1.3) has a fixed length *b*, lies at a variable angle θ from the cylinder axis, and makes a fixed number of turns *n* around the cylinder [11]. The muscle length is $L = b\cos\theta$ and the diameter is $D = b\sin\theta\,/(n\pi)$. Therefore $D^2 = b^2\sin^2\theta\,/(n^2\pi^2) = b^2(1-\cos^2\theta)/(n^2\pi^2)$ and $\cos^2\theta = L^2/b^2$. Assuming that the strands and bladder have negligible thickness, cylinder volume is

$$V = \frac{\pi D^2}{4}L = \frac{\pi\frac{b^2}{n^2\pi^2}(1-\cos^2\theta)}{4}L = \frac{b^2(1-L^2/b^2)}{4n^2\pi}L = \frac{b^2L - L^3}{4\pi n^2} \qquad 1.2$$

Equations (1.1) and (1.2) allow us to calculate force as a function of length. The force is directly proportional to pressure [10]:

$$F = \frac{P}{4\pi n^2}(3L^2 - b^2) \qquad 1.3$$

Figure **Error! Reference source not found.**1.4 shows the relationship of equation (1.3), plotting length normalized by strand length b and force normalized by the maximum force. Force decreases as the muscle contracts (right to left on the graph), and reaches zero at the point of maximum cylinder volume when the length is $1/\sqrt{3}$ or 57.7% of L_{max}, a value that is independent of n. The negative (compression) forces that would theoretically occur at shorter lengths may be neglected in most cases because artificial muscles are generally attached so as to apply only tensile forces.

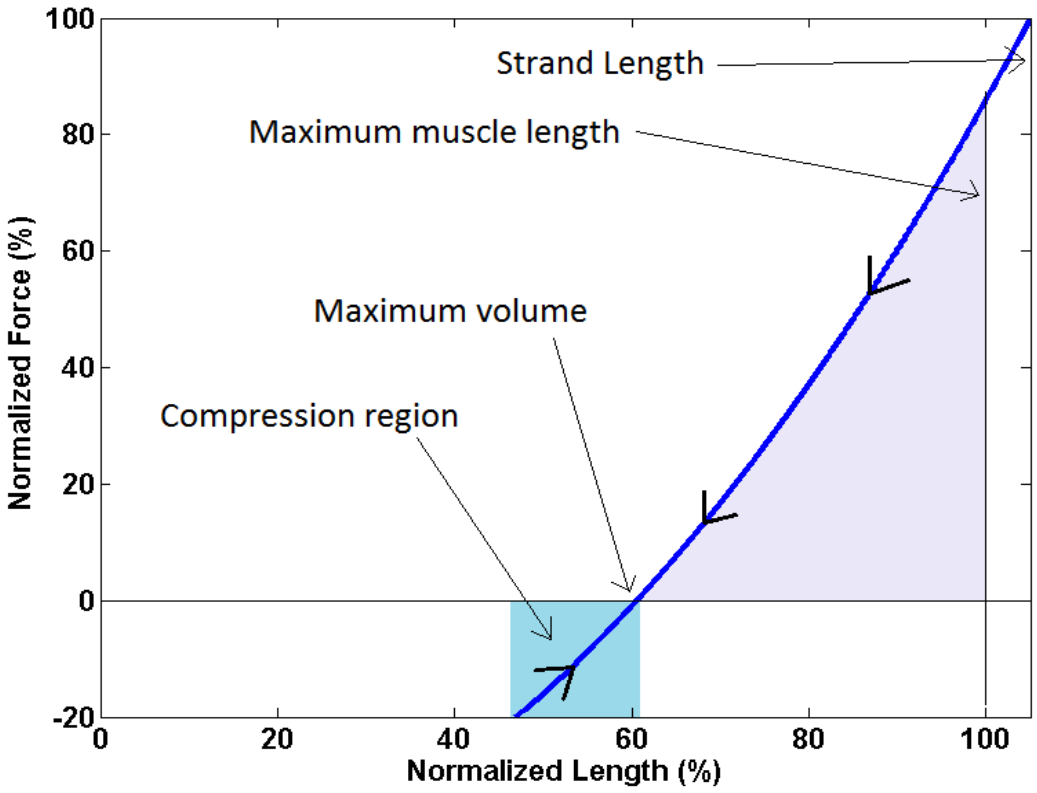

Figure 1.4: Normalized tension force as a function of actuator length, from the volume potential energy model.

Figure 1.4 is plotted for a McKibben muscle with initial braid angle zero and no bladder or sleeve thickness. In reality, no muscle can extend to its theoretical maximum length $L=b$ because its diameter would have to be zero, so there is some maximum length L_{max} with corresponding nonzero minimum values of θ and D; the far right portion of the ideal force curve in Figure 1.4 is unreachable.

1.3.2 Knitted-Sleeve Fluidic Muscle Ideal Force Model

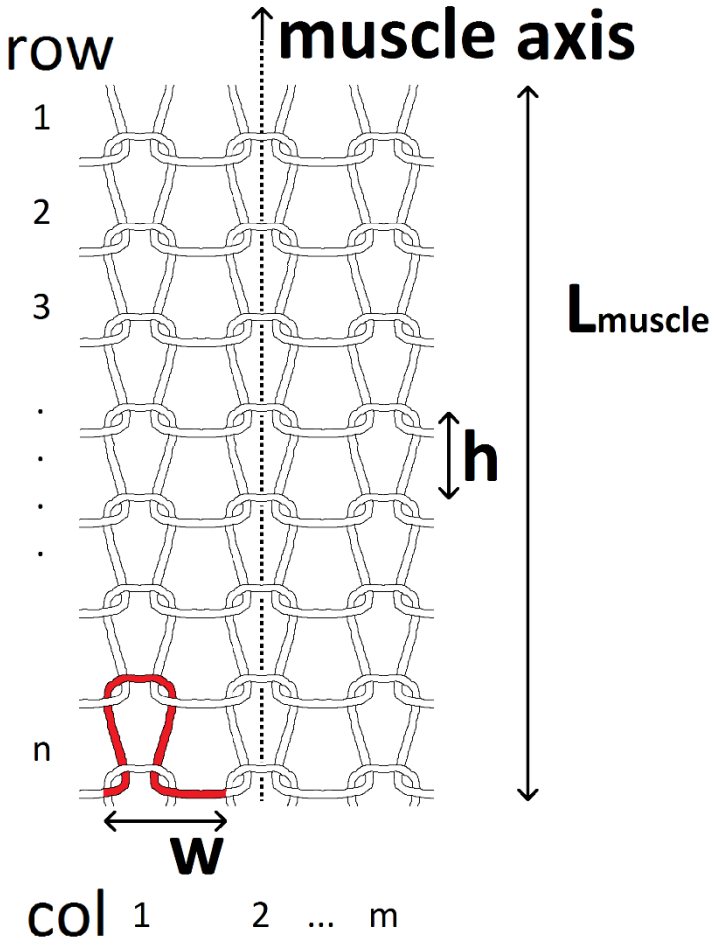

Figure 1.5: Diagram of a simple knitting pattern (stockinette stitch) with dimensions labeled.

As with the McKibben muscle, derivation of an ideal force curve for a knitted muscle requires specifying the geometric relationship between its length and its circumference, which together determine the volume as a function of contraction. In this case, instead of the sinusoidal relationship created by helical strands, the length and circumference are related linearly because each section of the strand is aligned either parallel or perpendicular to the muscle axis. Figure 1.5 shows the construction of the knitted sleeve and the variables used to describe the geometry. A single stitch is highlighted in red. In the simplest model, the sleeve consists of *n* rows, each made from a single strand that forms *m* stitches around the circumference of the muscle and has its ends connected to form a loop. The height of a stitch (and hence the distance between rows) is *h* so that the muscle length $L = nh$, and the width of a stitch is *w*, so that the circumference $C = mw$. Since each strand is inextensible, the length of strand in one row is a constant S_{row}. Adding up the lengths of each stitch in a row, it may be seen that

$$S_{row} = m(2h + w)$$
$$w = \frac{S_{row}}{m} - 2h \qquad 1.4$$

This equation for *w* in terms of *h* forms the basis for calculating muscle volume as a function of length. Substituting into the calculation of circumference one can find the radius, $r = \frac{mw}{2\pi} = \frac{1}{2\pi}(S_{row} - 2mh)$, and hence the volume,

$$V = \pi r^2 L = \frac{L}{4\pi}(S_{row} - 2mh)^2 \qquad 1.5$$

Expanding and substituting $L = nh$:

$$V = \frac{m^2 n}{\pi}h^3 - \frac{mnS_{row}}{\pi}h^2 + \frac{nS_{row}^2}{4\pi}h = \frac{m^2}{\pi n^2}L^3 - \frac{mS_{row}}{\pi n}L^2 + \frac{S_{row}^2}{4\pi}L \qquad 1.6$$

$$\frac{dV}{dL} = \frac{3m^2}{\pi n^2}L^2 - \frac{2mS_{row}}{\pi n}L + \frac{S_{row}^2}{4\pi} \tag{1.7}$$

Again, taking force to be proportional to the derivative of work done by the fluid source:

$$F_{ideal} = -P\frac{dV}{dL} = -\frac{P}{4\pi n^2}(12m^2L^2 - 8mnS_{row}L + n^2S_{row}^2) \tag{1.8}$$

Thus, the force output is again quadratic in L, but instead of using one leg of an upward parabola, the knitted muscle force curve is a downward parabola with its peak in the center of the stroke range, as illustrated in Figure 1.6. Therefore, it crosses zero at two different points, one at the point of maximum volume and one at full extension.

To determine the free contraction (contraction with no load), one can calculate the length of the muscle at which its volume is maximized by setting the derivative equal to zero, which yields two solutions:

$$\begin{gathered}\frac{dV}{dL} = 0 = \frac{3m^2}{\pi n^2}L^2 - \frac{2mS_{row}}{\pi n}L + \frac{S_{row}^2}{4\pi} \\ L_{free} = \frac{1}{3}\frac{nS_{row}}{m} \pm \frac{nS_{row}}{m}\sqrt{\frac{1}{9} - \frac{1}{12}} = \frac{nS_{row}}{m}\left(\frac{1}{3} \pm \frac{1}{6}\right)\end{gathered} \tag{1.9}$$

Since the maximum height of a row (when the muscle is fully stretched) is $h_{max} = \frac{S_{row}}{2m}$, as obtained from Equation (1.4), the stretched muscle length is

$$L_{max} = nh_{max} = \frac{nS_{row}}{2m} \tag{1.10}$$

Combining those and choosing the solution at which volume is maximized, it is found that $L_{free} = L_{max}/3$, one third of the stretched length. Therefore, the ideal knitted muscle could contract by up to 67%, compared with 42% for an ideal McKibben muscle.

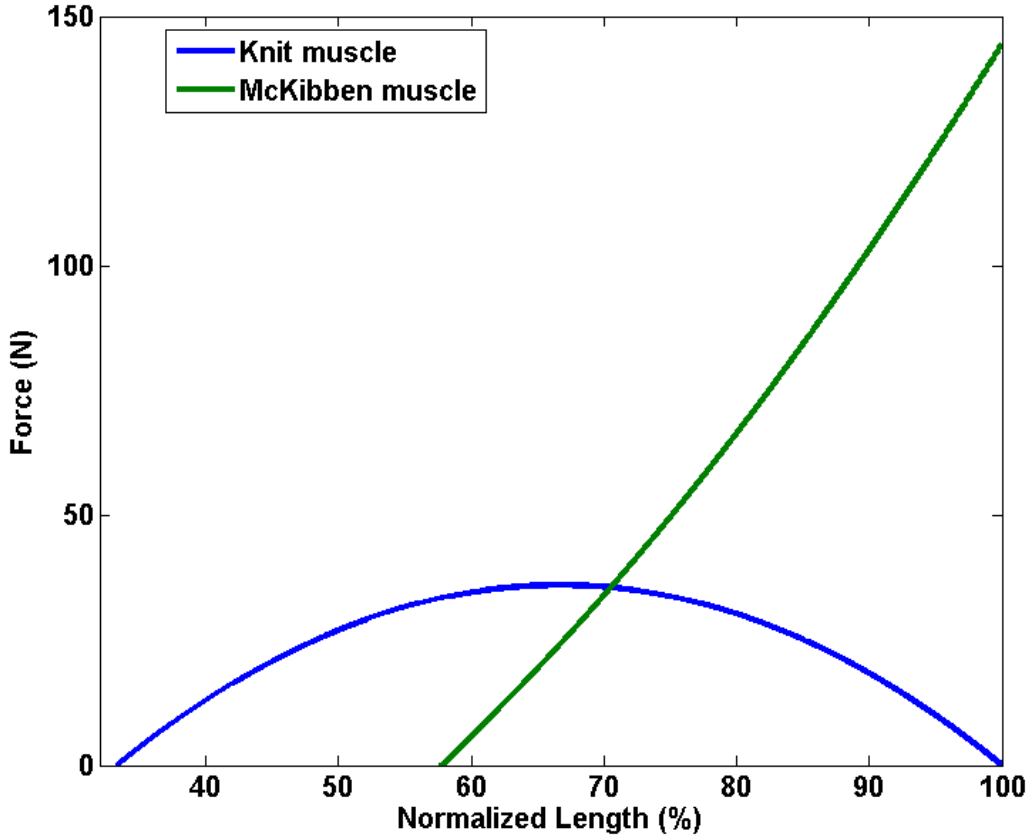

Figure 1.6: McKibben and knit muscle ideal force curves, each with diameter 13.3 mm at free contraction.

1.3.3 Tubular-Knit Model

The model above assumes that each row of the knitted sleeve consists of a separate yarn loop. In practice, there is no easy way to assemble such loops into a knitted tube. Instead, one may employ the technique known as tubular knitting or "knitting in the round," which is commonly used for making socks and other cylindrical fabric items. Instead of each row

connecting to itself, the end of one row becomes the beginning of the next row, so that the entire piece is actually made from a single strand of yarn, making this design easy to produce on a common knitting machine. However, it also invalidates the assumption that each row runs circumferentially, perpendicular to the muscle axis. Instead, the stitches go around in a gradual spiral, with each section at a slight angle compared to the circumference (Figure 1.7).

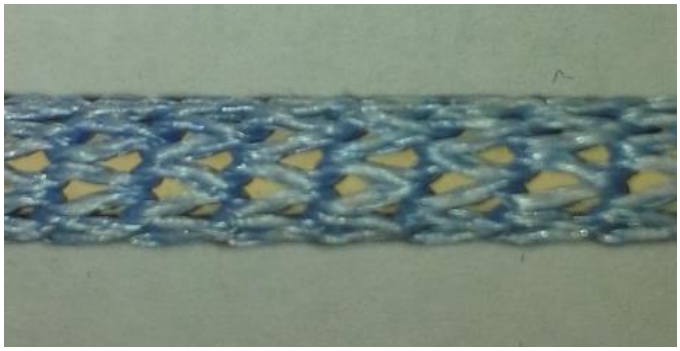

Figure 1.7: Tubular-knit sleeve, m = 8

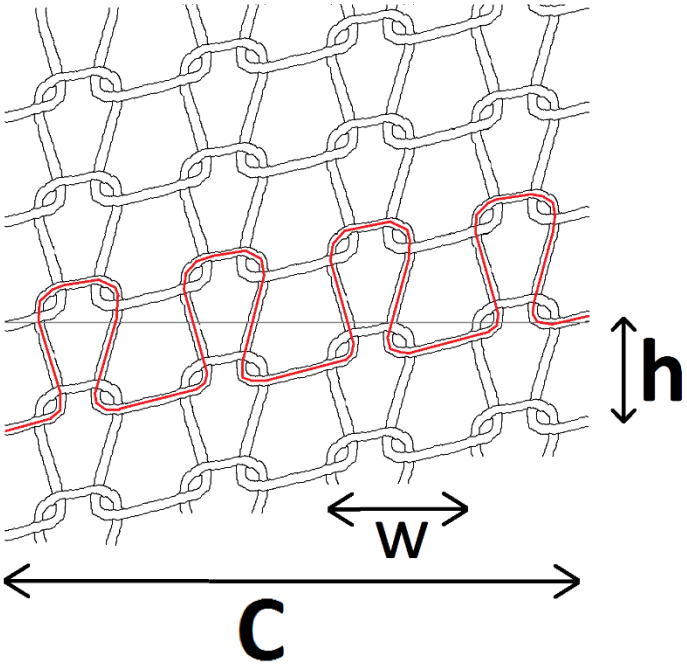

Figure 1.8: Diagram of flattened tubular-knit sleeve, m = 4. The strand length S_{row} is outlined in red.

Figure 1.8 shows this slanted configuration. The expression for the strand length in one row (Equation 1.4) must change to incorporate this slant. The vertical portions $2mh$ remains the same, but the previously horizontal portion is now the hypotenuse of a triangle with sides C, the circumference of the tube, and h, the height of the row:

$$S_{row} = 2mh + \sqrt{C^2 + h^2} \tag{1.11}$$

Substituting $C = 2\pi r$ and solving for r,

$$r^2 = \frac{1}{4\pi^2}(S_{row}^2 - 4mhS_{row} + (4m^2 - 1)h^2) \tag{1.12}$$

Therefore the tubular-knit muscle volume is

$$V_{tub} = \pi r^2 L = \frac{L}{4\pi}\left(\frac{1}{n^2}(4m^2 - 1)L^2 - \frac{4S_{row}m}{n}L + S_{row}^2\right) \tag{1.13}$$

and the force becomes

$$F_{tub} = -P\frac{dV_{tub}}{dL} = -P\frac{1}{4\pi n^2}\left((12m^2 - 3)L^2 - 8S_{row}mnL + n^2S_{row}^2\right) \tag{1.14}$$

The change in the force curve (Figure 1.9) is especially noticeable when the number of stitches per row is small, and may generally be neglected when $m > 16$. In some cases the increased initial force may be considered beneficial, though a similar effect can be achieved by increasing the minimum diameter.

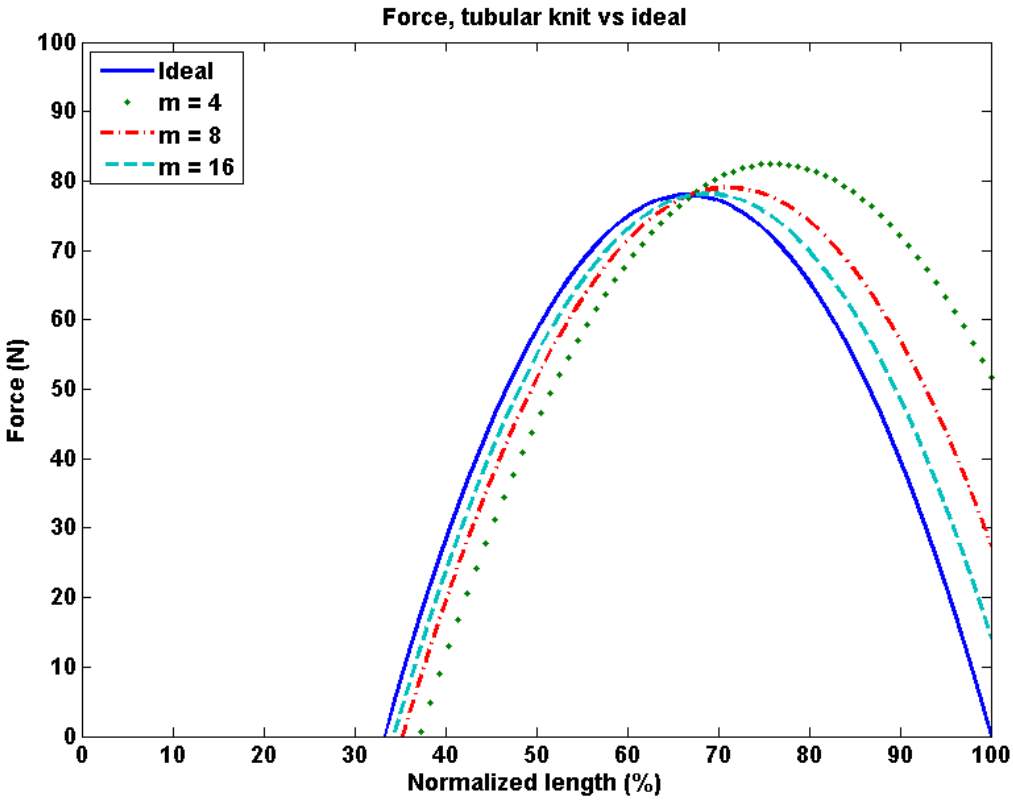

Figure 1.9: Tubular-knit sleeve force curves with different numbers of stitches per row, compared with the ideal force curve.

For the calculated curves in figure 1.9, the parameter *n* is adjusted so that each muscle would have the same diameter (97.9 mm) at free contraction, that is, the length where its volume is maximized. (This adjustment mimics a design requirement to fit within an opening of a given width.) As *m* increases, *n* must also increase (nonlinearly) in order to maintain a constant free contraction diameter. For a given value of *m*, a lower value of *n* will result in greater inflated diameter and therefore greater tensile force, which is why the curves with smaller *m* show slightly higher peak force. If instead the diameters were equal when fully stretched, peak forces would also be equal.

1.3.4 Thick Strand Model and Effect of Minimum Radius

A second major assumption of the ideal knit muscle force model is that the thread making up the sleeve is thin enough that its effect on the geometry of the sleeve may be neglected. To improve on this, consider the strand thickness *t*, which constrains both the length and the diameter of the sleeve, reducing the range of motion. Figure 1.10 shows how the length of strand in one stitch, S_{row}/m, is no longer equal to $2h+w$ as in the ideal model, but must include a correction for the thickness:

$$\frac{S_{row}}{m} \approx 2(2t + h) + w \qquad 1.15$$

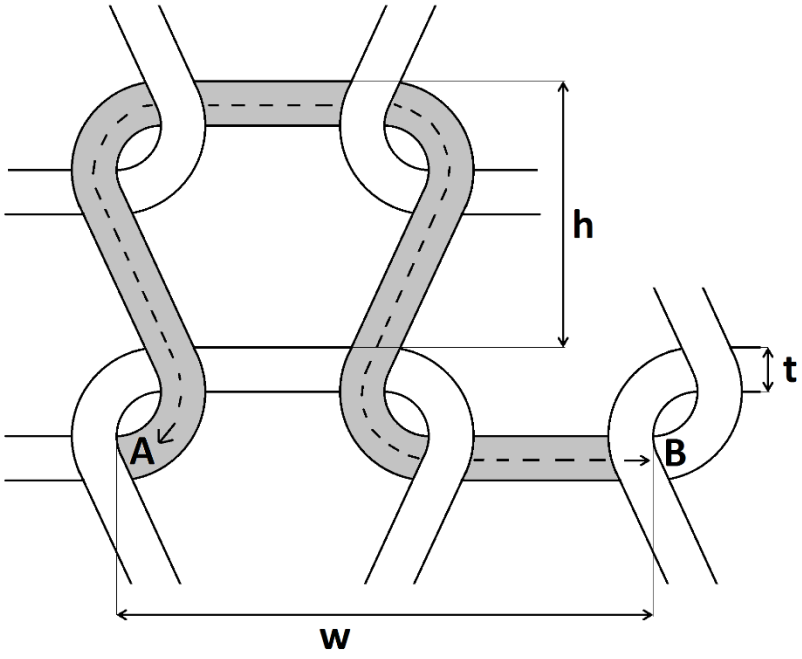

Figure 1.10: Diagram of a stitch with significant strand thickness. Indicated parameters are strand thickness *t*, stitch height *h*, and stitch width *w*. The length of the shaded section A-B is the length of strand section that forms one stitch, S_{row}/m.

Using this expression to calculate volume and force yields the same results as the ideal model, equations (1.6) and (1.8). However, it does impose a minimum radius on the sleeve at the length where the longitudinal strands are in contact with each other:

$$r_{min} = \frac{4mt}{2\,\pi} \tag{1.16}$$

This minimum radius prevents any real implementation of the knit muscle from reaching the far-right portion of the ideal force curve, just as with the McKibben muscle. If the radius of the bladder exceeds $\frac{4mt}{2\,\pi}$, then r_{min} will increase accordingly. The strand thickness also imposes a minimum length constraint $L_{min} = 2nt$, but in most cases this is well below the length at which volume is maximized and so has no practical effect. Figure 1.11 shows the ideal force curve compared with the force curve for a muscle with r_{min} equal to $\frac{4mt}{2\,\pi}$. Besides a reduction in the range of motion, the main effect is a large increase in the initial force when fully stretched.

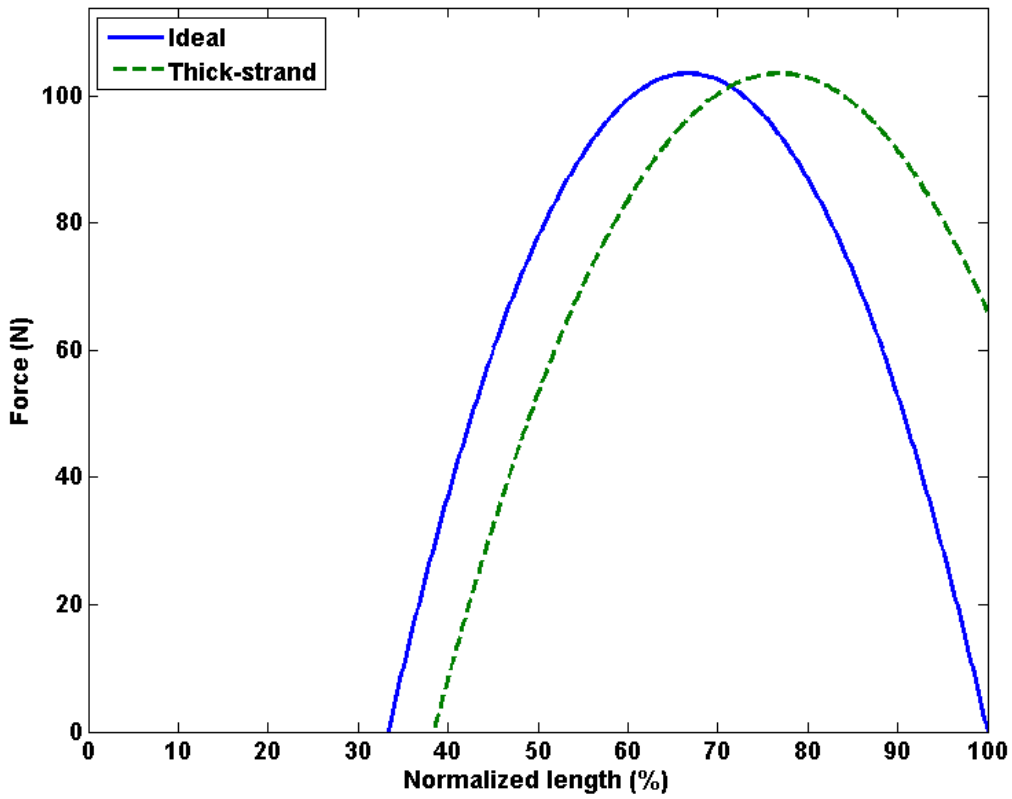

Figure 1.11: Force curve with minimum radius determined by strand thickness, compared with ideal force curve.

1.3.5 Effects of Non-Cylindrical Actuator Shape

The previous models all rely on the assumption that the sleeve geometry remains cylindrical throughout the stroke. There are two problems with this assumption. The first is that the clamps at each end of the sleeve constrain its diameter to a fixed value. This phenomenon is well documented in McKibben muscles and several models have been proposed to approximate its effect on volume and force [6,9,1,11,12]. In general, the effect is a reduction in both force and stroke length, particularly as the muscle approaches free contraction where the diameter is large.

The second cause of non-cylindrical sleeve geometry is unique to the knitted muscle design. As the actuator length begins to decrease from its full extension and its radius increases, the force initially increases as well. Force, in a pneumatic muscle, is the derivative of potential energy with respect to length, as discussed in section 1.3.1, and lengthwise contraction occurs because the gradient of potential energy leads the actuator to the configuration with minimum energy (maximum volume) for a given length. The radial expansion therefore occurs first in whatever region has the largest local derivative $\frac{dV}{dL}$. Since $\frac{dV}{dL}$ is proportional to force, this will also be the region where force generation is greatest—and so, initially, it will be the region with the largest radius. In contrast, a McKibben muscle, with force that monotonically decreases throughout the contraction, tends to expand in the area with the smallest radius, causing the radius to remain roughly equal everywhere except near the ends where it is constrained. The same effect that stabilizes the McKibben muscle radius creates an instability in the radius of the knitted muscle, causing a pocket of expanded radius to nucleate and grow while the rest of the length remains at its minimum radius (Figure 1.12 and Figure 1.13). This causes a divergence from the cylindrical force model in the "descending limb" region, where force decreases as length increases. The parameters of Figure 1.12 are chosen to match those of the prototype shown in Figure 1.13.

Both non-cylindrical shape effects can be approximated simultaneously using a numerical gradient-following optimization to calculate the muscle shape that leads to maximum volume at any given length. The version implemented here is somewhat slow to compute. It calculates *r* separately for each row of stitches, beginning with all of them equal to r_{min}. The values of *r* at the endpoints remain fixed at r_{min} throughout. It then effects a

small decrease in length from full extension, gradually increases r everywhere until the geometric constraint on strand length is once again satisfied, and calculates two Jacobian matrices $\frac{\partial V}{\partial \boldsymbol{r}}$ and $\frac{\partial L}{\partial \boldsymbol{r}}$, where $\boldsymbol{r}$ is now a vector of length n.

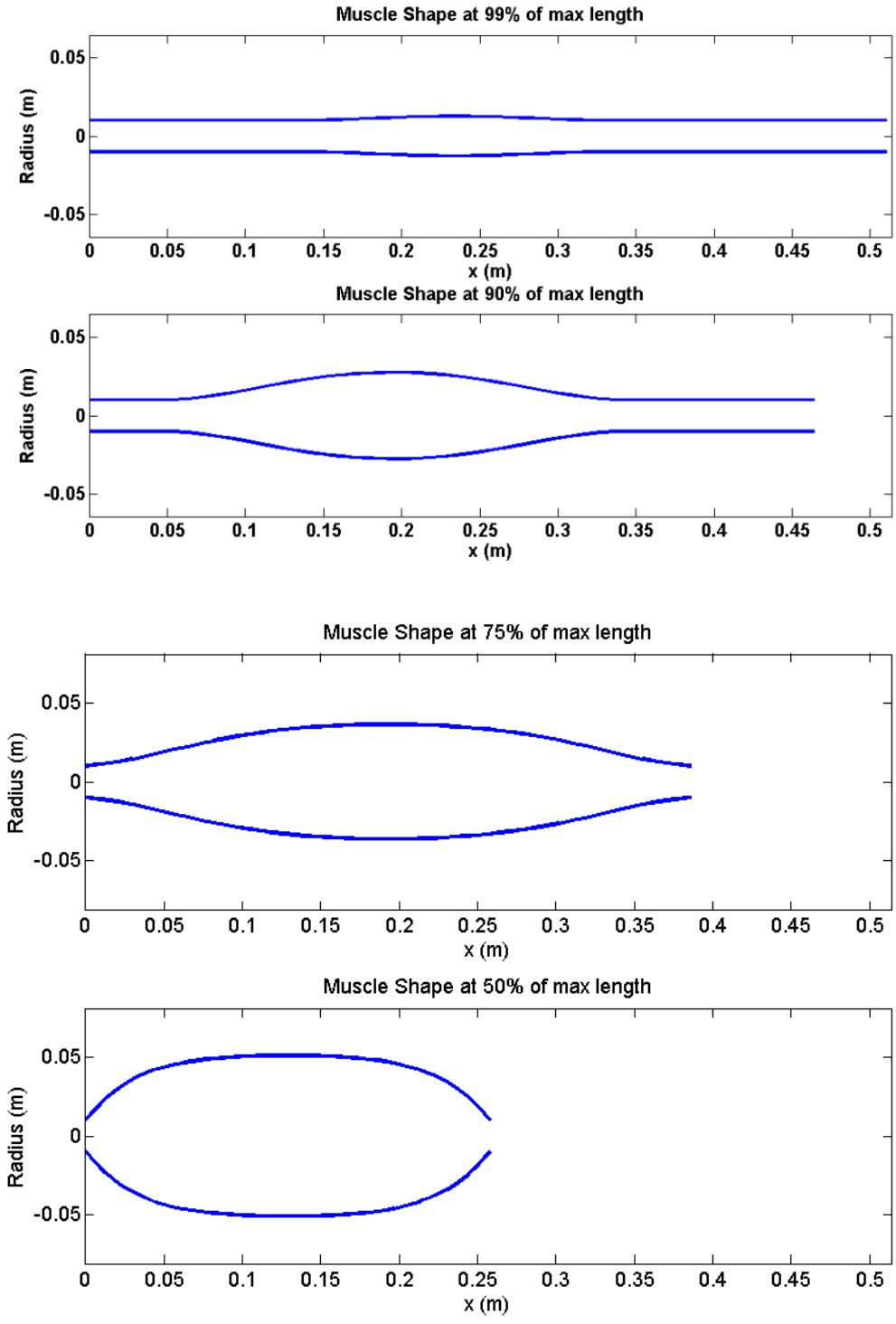

Figure 1.12: Predicted shape of knitted muscle at progressive stages in a contraction stroke.

These derivatives are calculated using the expressions

$$L_i = \sqrt{h_i^2 - (r_i - r_{i-1})^2} \tag{1.17}$$

which takes into account that the longitudinal segment *h* of the sleeve may be slanted, and

$$V_i = \frac{\frac{\pi}{3} L_i}{r_i - r_{i-1}} (r_i^3 - r_{i-1}^3) \tag{1.18}$$

which treats each segment as a truncated cone. Where *h* is relatively small (i.e. *n* is large) these approximations are valid; if *h* is large individual segments of the strand can be significantly curved due to pressure.

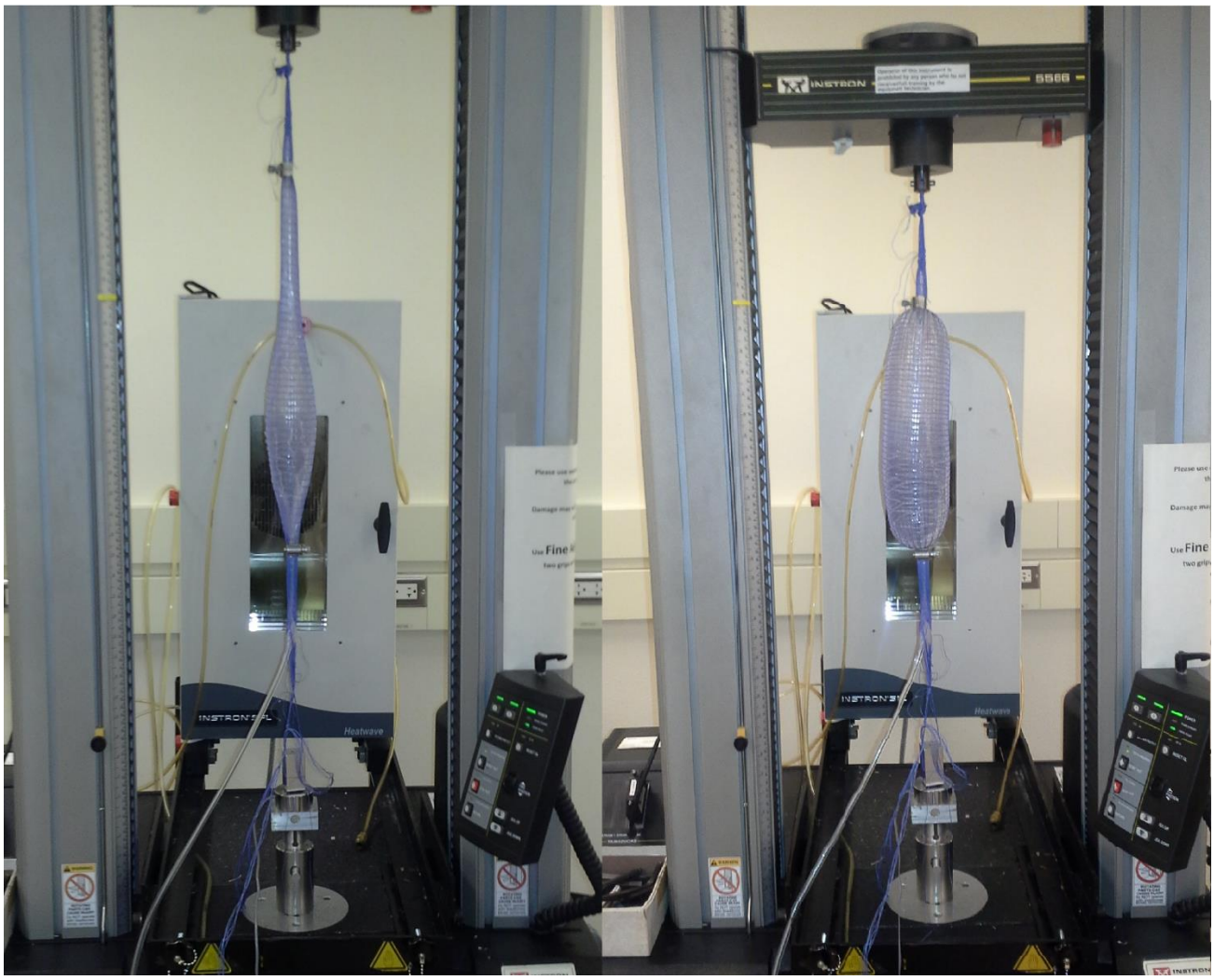

Figure 1.13: Actual shape of knitted muscle at progressive stages in a contraction stroke, demonstrating the instability effect.

In calculating the derivatives of L and V with respect to r of a particular row, which are too cumbersome to derive here, it is necessary to account for the changes in length and volume both of the row in question and of the following row, whose length and volume are affected by changes in the difference $r_i - r_{i-1}$:

$$\frac{\partial L}{\partial r_i} = \frac{\partial L_i}{\partial r_i} + \frac{\partial L_{i+1}}{\partial r_i} \qquad 1.19$$

and equivalently,

$$\frac{\partial V}{\partial r_i} = \frac{\partial V_i}{\partial r_i} + \frac{\partial V_{i+1}}{\partial r_i} \qquad 1.20$$

Once the Jacobian matrices are calculated, they are divided to produce a third matrix $\frac{dV}{dL}$. This corresponds to the energy minimization gradient mentioned earlier. The row with the highest value of $\frac{dV}{dL}$ is the one with the greatest tendency to expand. The next step in the algorithm, therefore, is to increase *r* at that point. The corresponding decrease in *L* is offset by a decrease in *r* at the point with the lowest value of $\frac{dV}{dL}$ and therefore the least tendency to expand (excluding, of course, rows where $r_i = r_{min}$ already). This process is repeated until all the values of $\frac{dV}{dL}$, except those where $r_i = r_{min}$, are approximately equal, indicating that the energy has been minimized. Then length can be marginally decreased again and the process continues until the volume as a function of length has been calculated for the entire contraction distance, that is, until volume reaches a maximum and begins to decrease again.

Figure 1.14 shows the results of this detailed prediction compared with the simple thick-strand model given above. The divergence is most prominent at the tail end of the ascending limb where the total stroke length is substantially reduced by end effects (along with total force and volume). There is also divergence on the descending limb portion of the force curve (the right side of the figure), where the non-cylindrical effect causes force to increase much more rapidly once the contraction begins but then to level off at a lower peak value. The end effects become less pronounced when the aspect ratio of the actuator (maximum length over maximum radius) is increased.

Figure 1.15 compares the instability effect on the ascending-limb force curve in two different simulated muscles with different values of r_{min}. The effect increases in importance when r_{min} is small.

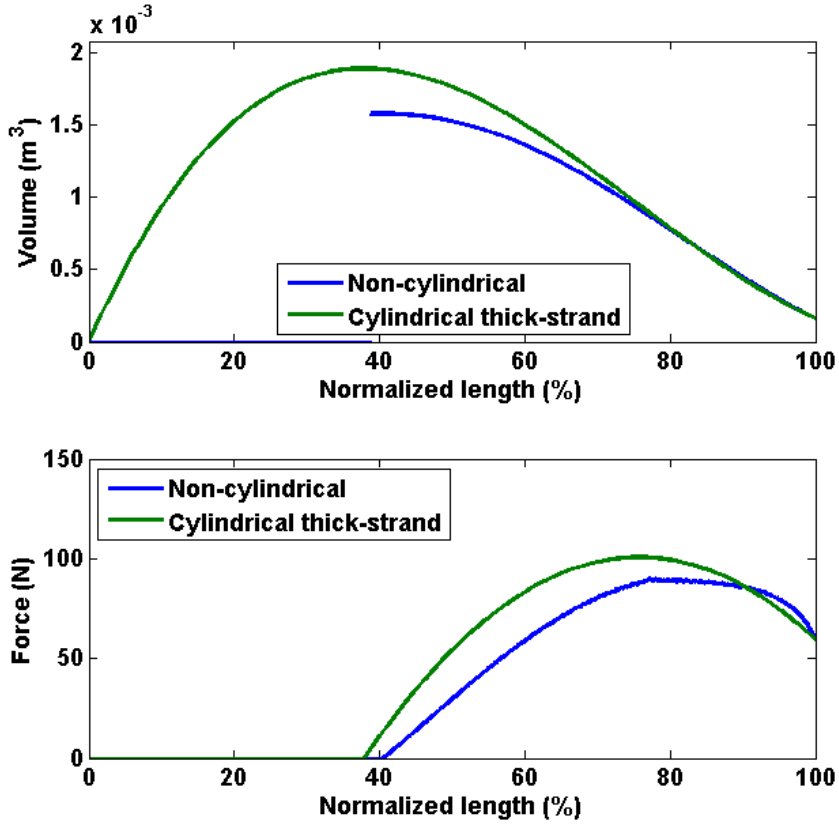

Figure 1.14: Volume and force curves resulting from non-cylindrical volume minimization, compared with cylindrical model.

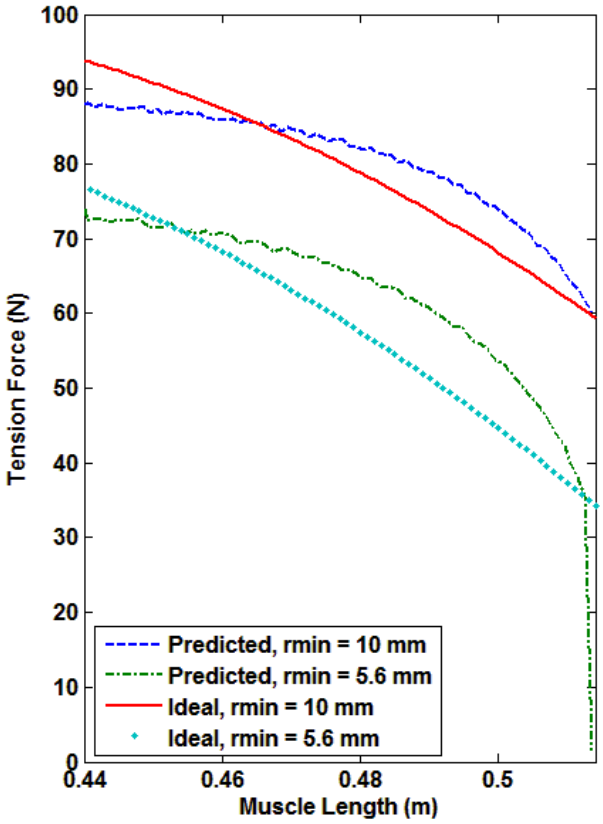

Figure 1.15: Comparison of numerically predicted force values (including instability effect) with thick-strand cylindrical model for different values of r_{min}.

1.3.6 Inclusion of Bladder Effects

The inclusion of a rubber bladder with non-negligible thickness, along with its effect on the force output of the actuator, has been thoroughly studied for McKibben muscles [6,10,16,17]. The same results apply to a knitted muscle, and applying the methods of [17] to the thick-strand knitted muscle model results in a force curve that is lower overall, with reduced free contraction, but higher initial force near maximum length. Pre-straining the bladder could potentially increase actuator force and stroke [17]. Figure 1.16 shows predicted

force-displacement curves for a 110 mm knitted-sleeve fluidic artificial muscle, maximum diameter during stroke 14.6 mm, at 550 kPa (80 psi). The blue curve is the ideal geometric case in which the bladder and strand thicknesses are insignificant, and reaches 67% displacement. The green curve includes the effects of a thick-walled rubber bladder with no pre-strain, with 0.2 mm strand thickness. Both curves neglect the tubular-knit correction from section 1.3.3. The predicted work done in one contraction stroke is 2.6 J. The curve including bladder effects is normalized by its resting length rather than maximum length, so it can extend slightly beyond 100% when tension is applied.

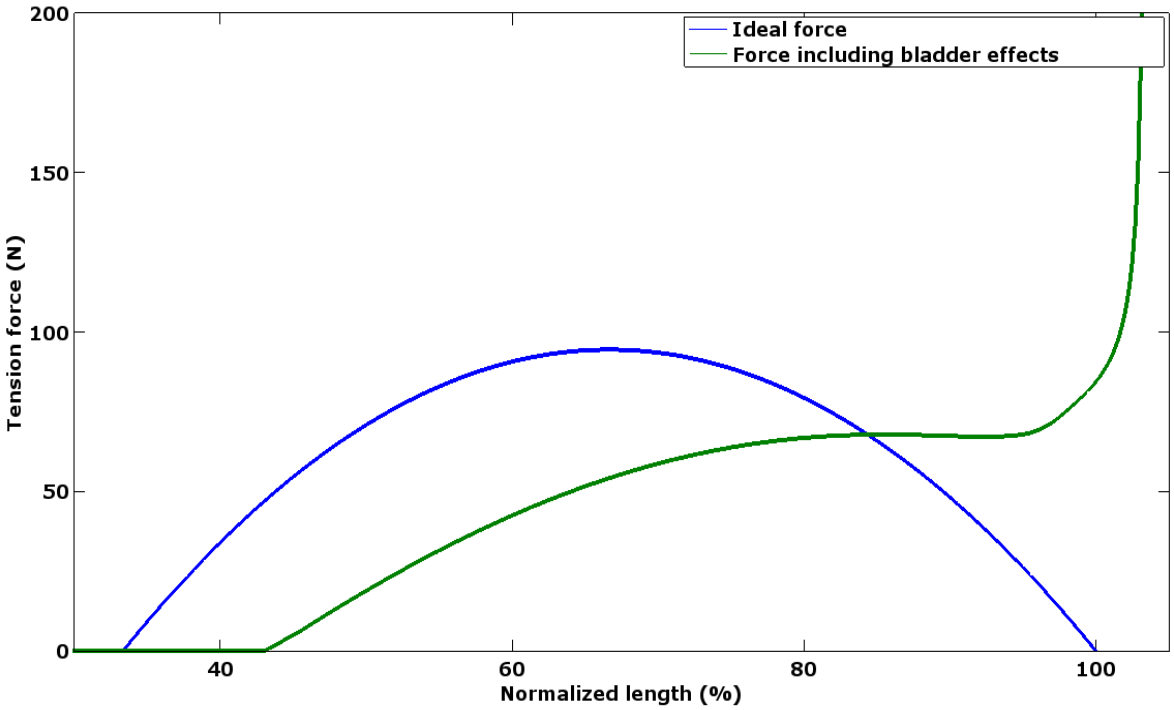

Figure 1.16: Predicted force-displacement curves for knitted muscle with and without bladder effects.

Figure 1.17 shows an equivalent plot for a traditional McKibben muscle with the same length, diameter, and pressure. Including bladder effects, the predicted work of one stroke is 2.3 J, which is less than the contraction work of the knitted muscle, even though an ideal McKibben muscle performs more work per stroke than an ideal knitted muscle. Peak force for the McKibben muscle is approximately twice that of the knitted muscle.

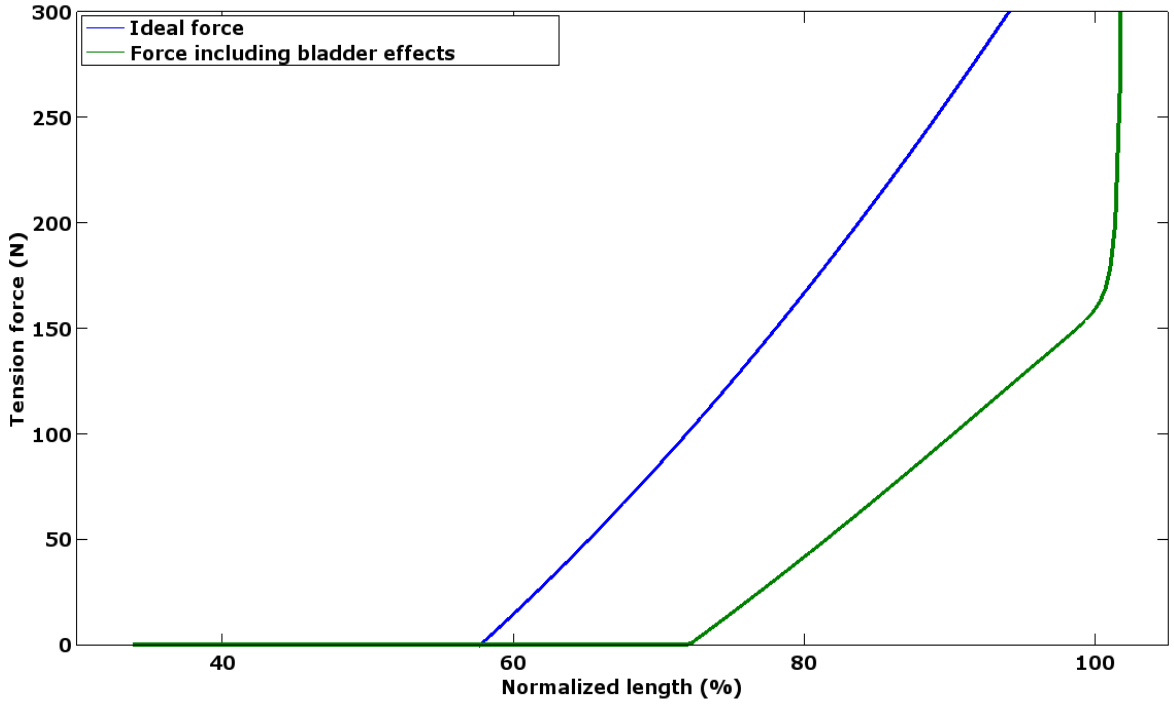

Figure 1.17: Predicted force-displacement curves for McKibben muscle with and without bladder effects.

1.3.7 Friction

A simple model for friction assumes that all friction occurs at the strand crossings and that tension everywhere in the strand is equal. Therefore the energy dissipated by friction is proportional to the number of crossings $2mn$, the length of the sliding motion at each crossing

$\Delta h = \Delta L/n$, and the strand tension $F_{strand} = (F_{muscle} + PA)/2m$. In this model, the friction force does not depend on the number of stitches per row or the number of rows in the sleeve. If we take the coefficient of friction to be C_f and the normal force at each right-angle crossing to be $2\ F_{strand}/\sqrt{2}$, because the two ends of the strand each protrude at a 45-degree angle to the normal force, then the total work expended on friction is

$$W_{friction} = \sqrt{2}(F_{muscle} + PA)C_f \Delta L \qquad 1.21$$

In this case the contribution of friction to actuator force is linear with the total actuator force. Realistically, several factors complicate this model. Substantial friction may occur between the sliding strands and the bladder, which would be proportional to pressure rather than strand tension. Pressure from the bladder may increase the friction between strands beyond what the tension force between them predicts. Finally, the assumption of constant strand tension is only approximately valid: end effects cause strand tension to increase where there is a radial component of tension as well as an axial component. Determining the magnitude of this effect is not attempted here. Figure 1.18 shows the force curve from the non-cylindrical in Figure 1.14, modified to include the predicted friction forces during extension and contraction (assuming $C_f = 0.25$). Bladder effects are not included. The extension curve begins at the point where the contraction force goes to zero. It is clear that a very low coefficient of friction is necessary to make the actuator operate efficiently.

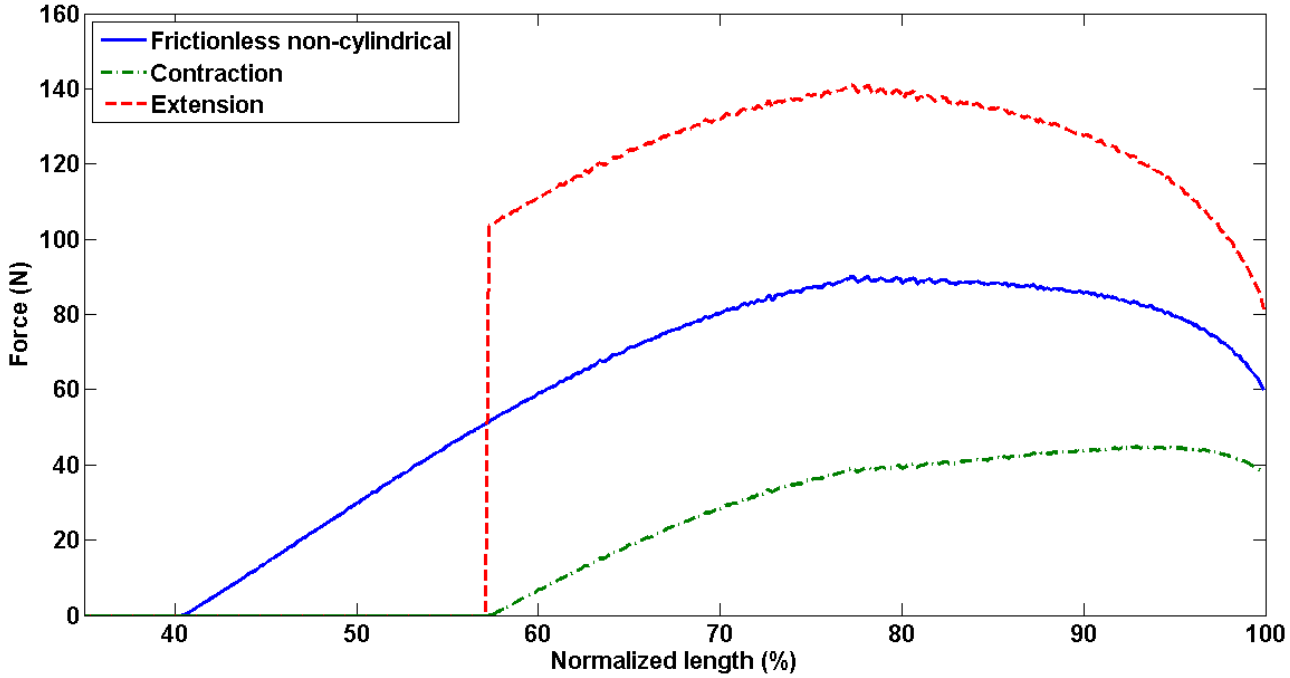

Figure 1.18: Predicted contraction and extension force curves with a simple friction model.

1.4 Muscle Testing

A prototype knitted muscle was constructed for quasi-static testing, using the tubular-knitting technique described in section 3.2. Figure 1.19 shows the knitting machine used for this purpose, an Addi Express Professional with 22 needles. The "yarn" must be thin and made from an inextensible high-modulus fiber to best approximate the ideal model; Spectra (UHMWPE) braided fishing line, rated for 220 N (50 lbf) was chosen as the strand material. UHMWPE is advantageous because of its combination of high stiffness and strength (allowing it to be thin) and its low coefficient of friction to reduce hysteresis.

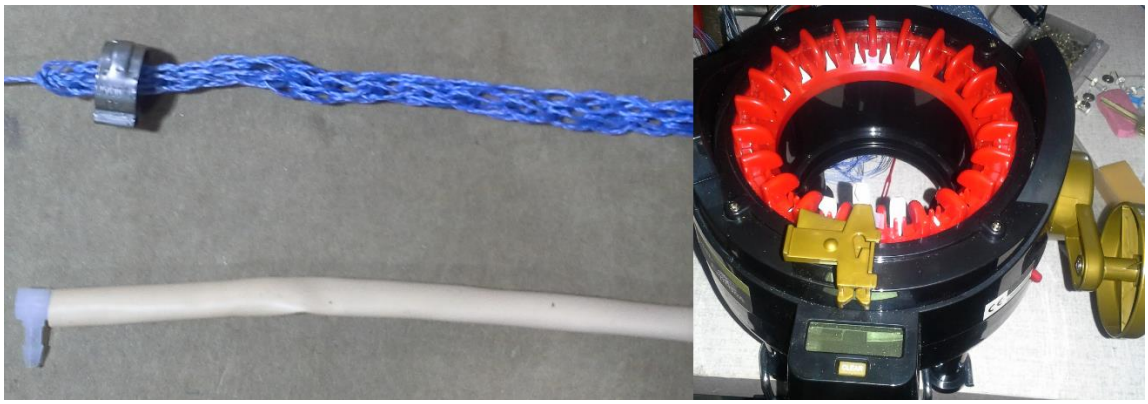

Figure 1.19: Components of a knitted-sleeve muscle prior to assembly. Top left: knitted sleeve and clamp for small prototype knitted muscle. Bottom left: Rubber bladder with pressure inlet at one end. Right: knitting machine used for large prototype.

Instead of the normal latex tube bladder, this prototype used a thin polyethylene bag membrane, in order to reduce passive force effects from stretching of the bladder [18]. Note that unlike a McKibben muscle, bonding the bladder to the sleeve or using a rubberized sleeve is not an option, as this would prevent the sliding motion of the sleeve threads necessary for contraction of the actuator.

The bladder was placed inside the sleeve and connected at the ends by circular clamps. A simple barbed hose fitting was clamped into one end to allow the application of pressurized air. The bladder was cut slightly shorter than the sleeve so that extra material was available at the ends (outside the clamps) for tying into mounting points on the object to be actuated (Figure 1.20). This attachment method allows tensile force to be transmitted through the stiff fibers directly, and does not rely on clamp friction to prevent stretching of the actuator. The prototype had a stretched length of 514 mm, $m = 22$, $n = 49$, maximum sleeve diameter

(before assembly) 153 mm, and maximum bladder diameter roughly 85 mm. Even when fully pressurized with no load, the muscle never reaches the maximum sleeve diameter because its diameter stops increasing when it nears the maximum possible volume.

Figure 1.20: Loaded test prototype pressurized to three different levels of contraction (0-15 kPa).

1.4.1 Experimental Setup

The prototype knitted muscle was tied into a tensile testing machine consisting of a hydraulic positioner and a load cell (Figure 1.21). Quasi-static tensile tests were performed over the stroke length of the actuator on both the contraction and extension strokes in order to

validate the theoretical force curves and estimate hysteresis. All tests were performed with the muscle pressurized to approximately 14 kPa (2 psi) with air. Crosshead speed was 150 mm/minute for both extension and contraction.

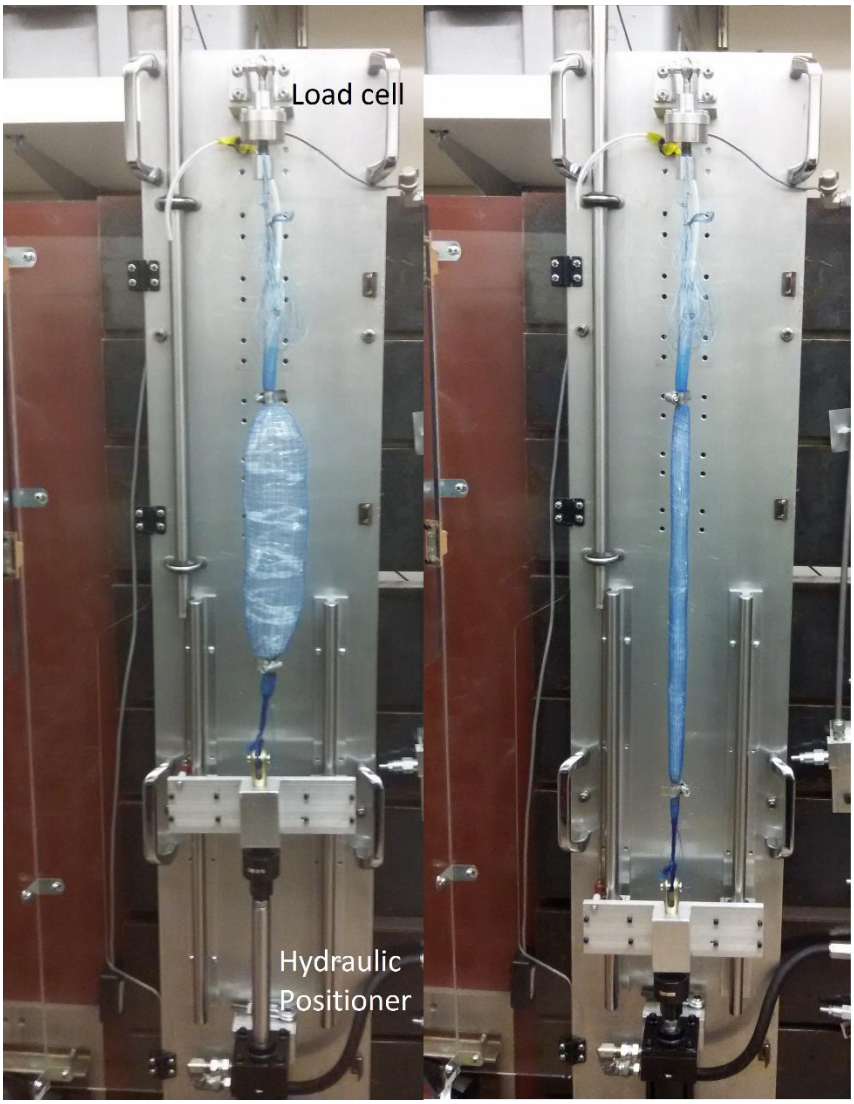

Figure 1.21: Tensile test setup: a) contracted, b) lengthened.

1.4.2 Results

Figure 1.22 shows the result of tensile testing and the corresponding theoretical prediction (using the computer model from section 3.5, which neglects friction). The

extension force curve is an average of six tests; the contraction force curve is an average of 19 tests. The extension force is less important to the evaluation of the design because an artificial muscle is normally pressurized during contraction in order to do work. Force values varied quite widely among these repetitions despite efforts to maintain the same test conditions.

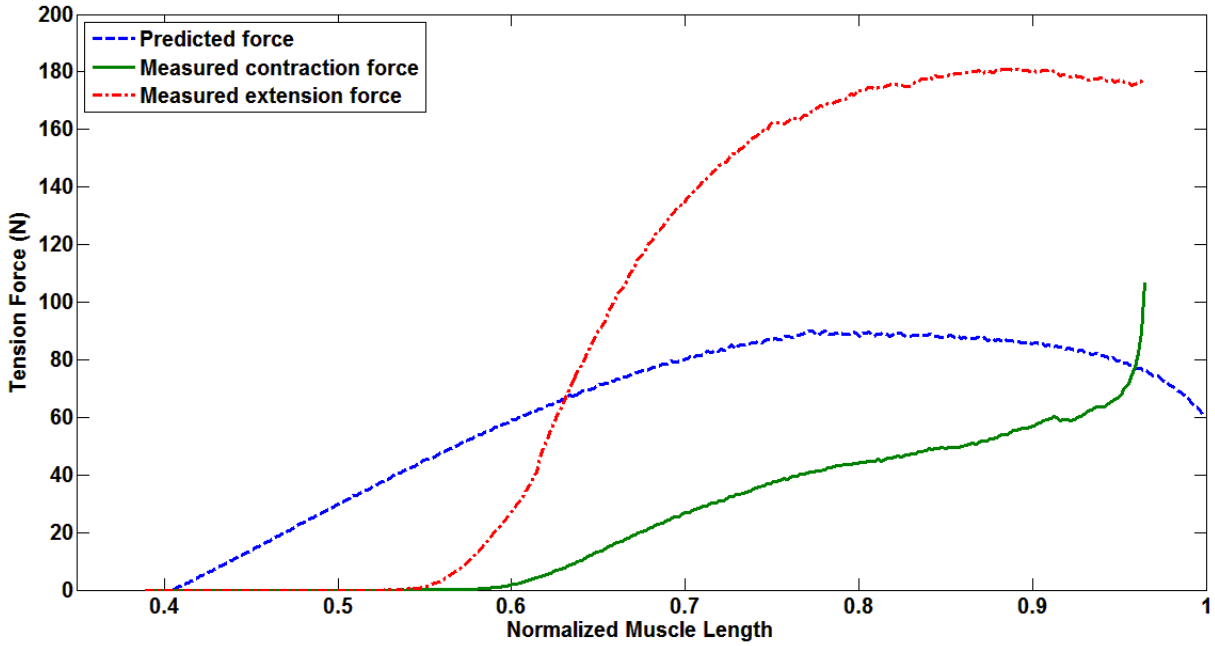

Figure 1.22: Tensile test results (extension and compression) compared with prediction, at 14 kPa (2 psi).

In addition, free contraction at 100 kPa (15 psi) was measured to be 51%. The increased contraction at higher pressure is likely due to stretching of the polyethylene bladder.

1.4.3 Analysis

Figure 1.22 demonstrates several ways in which the prototype's force curve diverges from the theoretical prediction. First, extension force is nearly three times as high as contraction force at the same pressure, implying that friction has a more significant effect in

this prototype than in a typical McKibben muscle. The predicted force does fall between the extension and contraction curves over most of the range of motion, as expected.

Second, the contraction data do not show force that is below the peak force value when the muscle is near its maximum length. Instead, the force is dramatically higher just below full extension. This difference may be attributed largely to the polyethylene bladder's resistance to full compression. The inconsistent folding and unfolding of the bladder is likely also responsible for much of the variation between repetitions and some sudden spikes or drops in force during tests. A latex bladder would provide greater consistency, and improve the fit between data and model.

Lastly, maximum contraction in these tests is significantly lower than predicted, by about 14% of maximum length. A small part of this (less than 1% of length) is due to neglecting the tubular-knit correction in the model. An unexpectedly short contraction stroke could also be due to the muscle reaching the expansion limit of the bladder; however, in that case a sudden drop in force would be expected at one specific diameter rather than a gradual trailing-off as these data show. Therefore the majority of the discrepancy in contraction distance is due to friction. This conclusion is supported by the observation that increased pressure increases contraction stroke length (51% contraction at 100 kPa versus 42% contraction at 14 kPa), because additional energy is available to overcome friction forces. It is roughly consistent with the predicted contraction curve in Figure 1.18, although no data is available for the coefficient of friction in this prototype.

The extension curve shows no force until it reaches approximately 54%, well beyond where the model predicts the force should become positive. This is consistent with the explanation that friction causes the reduced stroke length, despite the fact that friction

generally increases force during the extension stroke, because no compressive force was applied during these tests, so the actuator never actually compressed below the free contraction length it reached during the contraction stroke. Future compression tests might confirm that after forced compression below the predicted free contraction length, extension force will begin to increase at a shorter length.

1.5 Discussion

The knitted muscle may be easily used in any of the devices where McKibben muscles are traditionally used, and especially where space is constrained, since a shorter knitted-sleeve muscle can generate the same stroke length as a longer braided-sleeve muscle. Applications include prosthetics and other medical devices, industrial automation, aerospace vehicle actuators, and robotics.

A McKibben muscle has very high blocked force because at full length, its circumference varies as $\sin\theta$ and rises quickly with a slight increase in braid angle, but its length varies as $1 - cos\theta$ and so changes hardly at all with the initial increase in angle—thus, an initial small decrease in length comes with a large volume increase. But the force drops off quickly once the muscle contracts slightly, so when the McKibben muscle is employed to lift a constant load, or to tension a spring, the initial high force is wasted. Once the force falls below the load, the rest of the stroke is unuseable. These disadvantages may be mitigated by the use of cams or linkages, which add weight and complexity to a device.

Because the knitted muscle force curve is flatter than that of a McKibben muscle, and in fact the actuator force may rise somewhat during the initial portion of the stroke, knitted-sleeve muscles are more appropriate for use in series with linear springs and for actuating

constant loads. Despite its lower maximum force and lower energy output per stroke, under the right circumstances the knitted muscle can employ that energy more efficiently to pull a weight or spring a greater distance. As with McKibben muscles [19], energy efficiency can be improved by bundling several actuators and pressurizing only as many as needed for a given task. When any artificial muscle is used to actuate a joint, the torque can be made constant by changing the lever arm of the attachment point to balance the change in actuator force. But for a McKibben muscle, the necessary changes in lever arm or cam radius are much more extreme than for the relatively constant force output of a knitted muscle.

The primary disadvantages of the knitted muscle stem from the fact that its motion occurs by sliding the strands of the sleeve against each other under tension. This causes friction, which can be mitigated somewhat by the use of low-friction materials and possibly by lubrication. Fatigue life has yet to be determined, but wear on the sleeve strands could prove to be a problem over large numbers of cycles, as it has been in some McKibben muscles [20]. Later improvements largely eliminated this problem for McKibben muscles and the same may be possible for McKibben muscles [21]. The sleeve mesh is also vulnerable to distortion if one stitch is snagged and pulled out into a loop, so in some circumstances it may be advisable to use a protective fabric covering over the actuator.

Finally, knitted muscles have greater similarity to the behavior of animals' skeletal muscle than other types of fluidic artificial muscle. This can be favorable in situations where the actuator application mimics biology, including prosthetic limbs and biomimetic robotics. Figure 1.23 compares quasi-static force curves for animal muscles and fluidic artificial muscles. The animal muscles are normalized by resting length rather than maximum length,

so that when stretched they may have normalized length well over 100%. For this figure the normalizations of the artificial muscles have been adjusted to match.

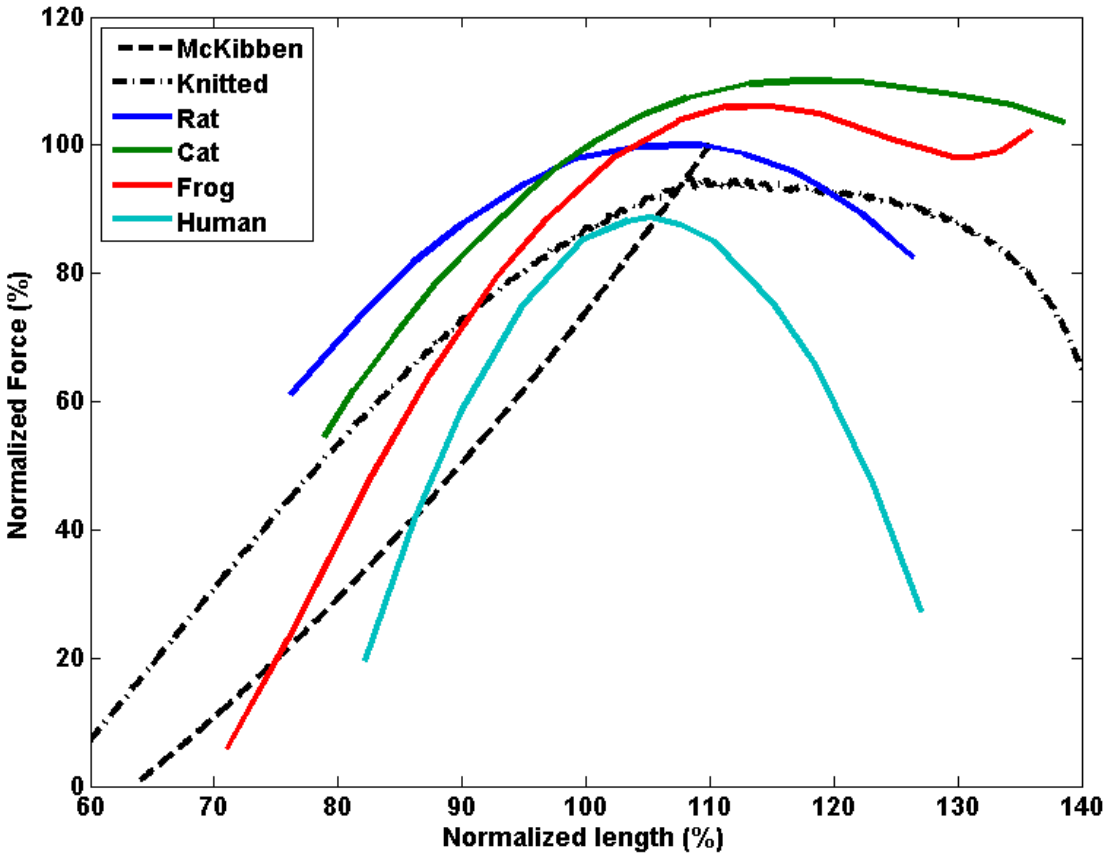

Figure 1.23: Comparison of fluidic artificial muscle force curves to biological muscle force curves. Based on data in [22].

Not only is the stroke length of a knitted muscle closer to that of animal muscle than a McKibben muscle, the stroke also has an extended plateau region in which force output is nearly constant. This plateau area is used extensively in skeletal motion [22]. Other fluidic artificial muscles have only an ascending limb (the leftmost portion of the force curve, in

which force increases steadily with length) leaving them unable to mimic some functions of animal muscle.

1.6 Conclusion

This paper has introduced the knitted muscle structure, a novel form of pneumatic artificial muscle, as a potential alternative to the McKibben muscle for applications that include robotics, prosthetics, and machinery that must interact with humans. Its operation is based on the sliding motion of strands through a knitted stitch to contribute either to length or to circumference of the muscle depending on the applied pressure. In addition to a simplified cylindrical model of the force curve, several corrections have been discussed including the effects of strand thickness, bladder material, and non-cylindrical shape. Experimental force curves diverge from the prediction. This deviation can be largely explained by the addition of substantial friction between the strands of the knitted sleeve, the greatest challenge for this design.

The principal advantages of the knitted muscle are its contraction length, increased by more than 50% compared to a McKibben muscle, and the relatively constant force output it produces through much of its range. The peak forces generated are low, and the design is both compliant amenable to performing significant work even at low operating pressures. These properties make it attractive for applications where human safety is a concern. Because of its greater contraction distance, the knitted muscle has the potential to perform similar motions to a McKibben muscle while occupying less axial space, adding less weight, and allowing looser tolerances in machine design. Furthermore, the better consistency in force output through the stroke can increase energy efficiency in cases of constant load, reduce joint size in rotating limbs, and improve the ability to simulate animal motion.

REFERENCES

[1] Tondu, B., “Modelling of the McKibben artificial muscle: A review,” J. Intelligent Material Systems and Structures 23(3): 225-253 (2012).

[2] Schroder, J., Erol, D., Kawamura, K., and Dillmann, R., “Dynamic Pneumatic Actuator Model for a Model-Based Torque Controller,” Computational Intelligence in Robotics and Automation, 2003, vol. 1, pp. 342-347, 2003.

[3] Ito, Akihito, Koh Kiyoto, and Nobuyuki Furuya. "Motion control of parallel manipulator using pneumatic artificial actuators." In Robotics and Biomimetics (ROBIO), 2010 IEEE International Conference on, pp. 460-465. IEEE, 2010.

[4] Daerden, F. and Lefeber, D., “Pneumatic Artificial Muscles: actuators for robotics and automation,” European Journal of Mechanical and Environmental Engineering 47 11-21, 2002.

[5] Hitchcox, A., “Telescoping cylinders go the extra distance,” Hydraulics & Pneumatics, 2006.

[6] Gaylord, R.H., “Fluid actuated motor system and stroking device”, US Patent No. 2844126, 1958.

[7] Abel, J., Luntz, J. and Brei, D., “Hierarchical architecture of active knits,” Smart Mater. Struct. 22, 125001 (2013).

[8] Schulte, H.F., Adamski, D.F., and Pearson, J.R., “Characteristics of the Braided Fluid Actuator,” Technical Report No. 5, The University of Michigan Medical School Department of Physical Medicine and Rehabilitation Orthetics Research Project, 1961.

[9] Chou, C.P., Hannaford, B., “Measurement and Modeling of McKibben Pneumatic Artificial Muscles,” IEEE Transactions on Robotics and Automation 12(1): 90-102 (1996).

[10] Tiwari, R., Meller, M. A., Wajcs, K. B., Moses, C., Reveles, I., and Garcia, E., "Hydraulic artificial muscles," J. of Intelligent Material Systems and Structures 23, 301-312 (2012).

[11] Kothera, C.S., Jangid, M., Sirohi, J., and Wereley, N.M., "Experimental Characterization and Static Modeling of McKibben Actuators," J. Mech. Des. 131(9), 091010 (2009).

[12] Niiyama, R. and Kuniyoshi, Y., "Super Long Stroke Pneumatic Artificial Muscle for Articular Mechanisms," ICRA Workshop on Biologically-inspired Actuation, 2011.

[13] Daerden, F. and Lefeber, D., "The concept and design of pleated pneumatic artificial muscles", International Journal of Fluid Power, vol. 2, no. 3, pp. 41–50, 2001.

[14] "Fluidic Muscle DMSP/MAS," Festo Corporation, 2013. www.festo.com/en-us_us/data/doc_enus/PDF/US/DMSP-MAS_ENUS.PDF

[15] Paynter, H.M., "High pressure fluid-driven tension actuators and methods for constructing them", US Patent No. 4 751 869, 1988.

[16] Klute, G. K., Hannaford, B., "Accounting for Elastic Energy Storage in McKibben Artificial Muscle Actuators," ASME J. of Dynamic Systems, Measurement, and Control, 122(2):386-388 (2000).

[17] Ball, E. and Garcia, E., "Effects of Geometric Variations on McKibben Pneumatic Artificial Muscles," Proc. SPIE, 2013.

[18] Klute, G. K., Hannaford, B., "Fatigue Characteristics of McKibben Artificial Muscle Actuators," Proc. IEEERSJ Int. Conf. on Intelligent Robots and Systems Innovations in Theory Practice and Applications, 98(36) 190 (1998).

[19] Bryant, M., Meller, M.A. and Garcia, E., "Toward variable recruitment fluidic artificial muscles," ASME 2013 Conference on Smart Materials, Adaptive Structures and Intelligent Systems (pp. V002T06A014-V002T06A014).

[20] Klute, G., Czerniecki, J., and Hannaford, B., "McKibben Artificial Muscles: Pneumatic Actuators with Biomechanical Intelligence," Int. Conf. Advanced Intelligent Mechatronics, 1999.

[21] Woods, B.K., Gentry, M.F., Kothera, C.S. and Wereley, N.M., "Fatigue life testing of swaged pneumatic artificial muscles as actuators for aerospace applications," Journal of intelligent material systems and structures, 23(3), pp.327-343, 2012.

[22] M. Meller, M. Bryant and E. Garcia, "Reconsidering the McKibben muscle: energetics, operating fluid, and bladder material," Journal of Intelligent Material Systems and Structures, vol. 25, no. 18, 2014.

CHAPTER 2

EFFECTS OF BLADDER GEOMETRY IN PNEUMATIC ARTIFICIAL MUSCLES

Abstract

Designing optimal pneumatic muscles for a particular application requires an accurate model of the hyper-elastic bladder and how it influences contraction force. Previous work does not fully explain the influence of bladder pre-strain on actuator characteristics. We present here modeling and experimental data on the actuation properties of artificial muscles constructed with varying bladder pre-strain and wall thickness. The tests determine quasi-static force-length relationships during extension and contraction, for muscles constructed with unstretched bladder lengths equal to 55%, 66%, and 97% of the stretched muscle length, and two different wall thicknesses. Actuator force and maximum contraction length are found to depend strongly on both the pre-strain and the thickness of the rubber, making existing models inadequate for choosing bladder geometry. A model is presented to better predict force-length characteristics from geometric parameters, using a novel thick-walled tube calculation to account for the nonlinear elastic properties of the bladder. It includes axial force generated by stretching the bladder lengthwise, and it also describes the hoop stress created by radial expansion of the muscle that partially counteracts the internal fluid pressure exerted outward on the mesh. This effective reduction in pressure affects both axial muscle force and mesh-on-bladder friction. The rubber bladder is modeled as a Mooney-Rivlin incompressible solid. The axial force generated by the mesh is found directly from contact forces rather than from potential energy. Modeling the bladder as a thin-walled tube gives a close match to experimental data on wall thickness, but a thick-walled bladder model is found to be necessary for explaining the effects of pre-strain.

2.1 Introduction

McKibben pneumatic artificial muscles have existed since the 1950s, originally intended to power prosthetics and assist weakened or paralyzed muscles [1] and later finding use largely in robotics research and bio-mimetic systems [2, 3, 4, 5]. They are simple to construct, inexpensive, and lightweight. A muscle consists of an expandable inner bladder (usually a rubber tube) designed to hold pressurized air, placed inside a braided (bias-woven) mesh sleeve that supports it. The cylindrical sleeve consists of thin helically wound strands that are flexible but inextensible, so that the cylinder may expand radially when pressurized but with a corresponding decrease in length via a pantograph mechanism, as shown in Figure 1. One end of the bladder is connected to an air source and the other is plugged. The unstretched bladder length may initially be shorter than the sleeve length, but the mesh is clamped firmly around the bladder at both ends to pre-strain the bladder so that the bladder length and sleeve length become identical. Although the clamps constrain the diameter near the ends, a muscle with length much greater than its diameter remains nearly cylindrical and minimizes tip effects [6]. Pressurizing the bladder causes it to press outward against the sleeve, which increases in diameter and contracts in length.

Figure 2.1: McKibben muscle actuation: a) unpressurized muscle at its relaxed length, b) the pressurized muscle expands in diameter but contracts in length.

Extensive analysis and analytical modeling of this basic design was performed early on by Gaylord and Schulte [7, 8, 9]. Though the McKibben muscle remains the most common, several variations and alternative designs of pneumatic and fluidic artificial muscles have since been developed [10, 11, 12] having different strengths and potential applications. These include versions where the inextensible strands curve outward instead of helically [13] and the pleated muscle [14] which reduces hysteresis by eliminating both the elastic bladder and the sliding friction between the strands. In addition to their high force-to-weight ratio, most pneumatic muscles share the crucial property of natural compliance, making them inherently safe to operate in close proximity with humans and therefore attractive for ubiquitous robotic devices [15, 16, 17].

The quasi-static force output of a McKibben muscle is generally similar to that of a biological muscle [13, 18], and the dynamic behavior can be modified using dampers and biomimetic “tendons” to better approximate the motion of biological muscle as well [5].

The practical utility of pneumatic muscles has been limited by several factors: limited service life in some implementations [19] though more recent work has shown drastic improvements [20], shorter stroke length than pneumatic cylinders, non-linearity of both the actuator force and the passive spring force, inability to actuate bidirectionally, and substantial hysteresis with associated energy losses [2]. Bandwidth is also limited, especially in large-diameter muscles, but can be improved by the use of various filler materials inside the bladder [22]. Control methods have been proposed to further improve on the safety, stability, and accuracy of pneumatic muscles via position and torque feedback, and to compensate for hysteresis [17, 23, 24]. Given the promising work to overcome the problems associated with them and the rapid advancement of the field of robotics, pneumatic muscles are likely to become more widely used in the near future.

When designing pneumatic muscles for a particular engineering task, it is beneficial to know how the actuator characteristics will vary with the choice of part sizes and configuration. In particular, we wish to optimize the bladder thickness, diameter, and pre-strain. Pre-straining the bladder before clamping it inside the sleeve is a common practice, with the intent of preventing any compressive stress in the bladder during contraction [25]. The ratio of bladder length to sleeve length has often been chosen by trial and error due to incomplete theoretical understanding of its effects, which we seek to remedy. Previous models have sought to explain the impact of a nonlinear bladder material on the force and work output of McKibben muscles using hyperelastic material models, but none have yet included a model of the bladder pre-strain [6, 26]. Expanding on our previous treatment of the subject [27], this work predicts the effects of bladder parameters on the important muscle properties: the tension produced for any given muscle length and gauge pressure, the degree

of hysteresis, the maximum stroke length, and the work performed in one cycle of the actuator.

A theoretical model suitable for muscle design is necessarily highly nonlinear and depends on a large set of geometric and material parameters. It is therefore excessively complex and unwieldy as a model of actuator force for planning dynamics and control methods of an entire robotic system, where linear models are more useful because they lend themselves to frequency-domain analysis [22]. Therefore, once the muscle design is finalized the model may be linearized to treat the muscle as a variable-stiffness spring, with stiffness proportional to applied pressure minus a threshold pressure [6]. Threshold pressure is the pressure at which the bladder (if not constrained by the sleeve) can inflate. The nonlinear elasticity of the bladder, in typical tube geometries, causes a discontinuity in the pressure-diameter relationship and allows its expansion to occur suddenly and dramatically above a certain pressure, an effect often observed when inflating cylindrical balloons. Above this threshold pressure the bladder begins to apply substantial outward force to the sleeve and therefore generate axial force. Threshold pressure increases with bladder thickness and modulus and decreases with bladder diameter. It is easy to determine experimentally from a finished muscle or to estimate from the model described in Section 2.2. The resulting linearized model can be reasonably accurate and in many cases may be appropriate for designing feedback loops and estimating the response of a system to disturbances.

Section 2.2 presents two quasi-static models for the force-length relationship: an ideal model that calculates potential energy based on the volume of the cylinder, and a new detailed model that considers the effects of elasticity in the bladder, treating it as either a thin-walled

or a thick-walled tube. Section 3 describes our testing of pneumatic muscles with varying geometries and shows the results. Section 4 compares test results with the theoretical models.

2.2 Quasi-Static Models

2.2.1 Volume Potential Energy Model

This idealized geometric model of a pneumatic muscle, often called the Gaylord force model, assumes a conservative system [18]. It therefore takes tensile force F to be the derivative of potential energy U with respect to the muscle length L. It accounts only for the potential energy of the pressurized fluid source, which depends on its gauge pressure P and the volume V of gas in the muscle:

$$F = \frac{dU}{dL} = -P\frac{dV}{dL} \qquad 2.1$$

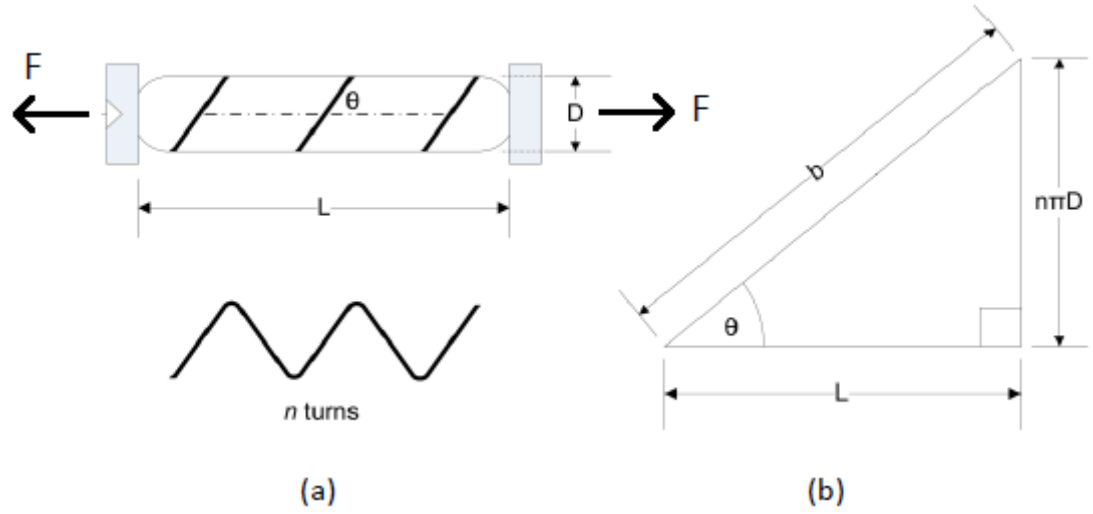

Figure 2.2: Sleeve geometry: a) helically wound strand forming part of the sleeve cylinder, b) unwound strand showing how the dimensions are related geometrically. Adapted from Tiwari and Meller [25].

The layout of the helical strands determines the relationship between length and volume. The muscle portion of each strand has fixed length b, and lies at a variable angle θ from the direction of the cylinder axis. It makes a fixed number of turns n around the cylinder, which remains constant when the actuator lengthens or contracts [18]. As Figure 2.2 shows, the cylinder length is $L = b\cos\theta$ and the diameter is $D = b\sin\theta\,/(n\pi)$. Then $D^2 = b^2\sin^2\theta\,/(n^2\pi^2) = b^2(1-\cos^2\theta)/(n^2\pi^2)$ and $\cos^2\theta = L^2/b^2$. If we assume the strands and bladder to have negligible thickness, the cylinder volume is

$$V = \frac{\pi D^2}{4}L = \frac{\pi\frac{b^2}{n^2\pi^2}(1-\cos^2\theta)}{4}L = \frac{b^2(1-L^2/b^2)}{4n^2\pi}L = \frac{b^2L - L^3}{4\pi n^2} \tag{2.2}$$

Combining Eqs. (2.1) and (2.2) we can calculate the force as a function of length that is directly proportional to pressure [6]:

$$F = \frac{P}{4\pi n^2}(3L^2 - b^2) \tag{2.3}$$

Error! Reference source not found. is a plot of this ideal relationship. The horizontal axis is the ratio of actuator length to strand length b, and the vertical axis is the ratio of force to maximum force. The force decreases as the muscle contracts (right to left on the graph), reaching zero when the length is $1/\sqrt{3}$ or 57.7% of the strand length. The intersection where the tension force reaches zero corresponds to the maximum volume of the cylinder inside the sleeve. The negative (compression) forces at shorter lengths are usually neglected because the muscle buckles easily.

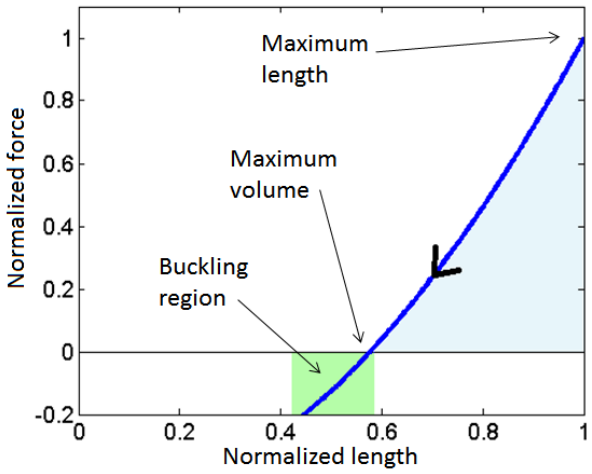

Figure 2.3: Normalized tension force as a function of actuator length from the volume potential energy model.

Schulte (1961) derived a model similar to the one just described, but rejected it in favor of empirical relationships because without modeling friction and rubber elasticity it could not accurately predict the behavior of the device [9].

In practice, the muscle cannot extend to the maximum theoretical length $L=b$ because its diameter would have to go to zero, so it has some maximum length L_{max} with corresponding minimum values of θ and D, and the rightmost portion of the ideal force curve is unreachable. This limit may be found experimentally, and in our tests, with bladder inner diameter 1.6 mm and outer diameter 4.8 mm, the limit is at approximately $\theta = 16°$, or $L_{max} = 0.96b$. If the volume occupied by the bladder increases because the bladder is thicker or less compliant, the maximum length of the actuator decreases.

2.2.2 Force Model Accounting for Bladder Material

The behavior of some large scale pneumatic muscles may approach the equations above, if a simple friction model is included. However, in small muscles (maximum sleeve diameter of a few centimeters or less) the effects of the bladder material become crucial. This is because the thickness of the bladder must be sufficient to contain the fluid pressure, a requirement that does not vary with muscle size but only with the spacing of strands in the sleeve. In our design, the sleeve is a mesh with relatively wide spacing, making bladder thickness even more important. If the bladder wall is too thin, failure can occur by expansion of the bladder through gaps in the mesh (Figure 2.4). In the case shown here, one end of the bladder has pushed itself out of the sleeve entirely. More commonly, a small piece of the bladder expands through a gap in the sleeve until it breaks and releases the fluid pressure. To prevent this when muscle diameter is small, the bladder wall thickness is proportionally greater. If the spacing of strands in the sleeve is much closer, as in a continuous fabric, the bladder is more likely to fail by fatigue or repeated friction against the sleeve or clamping mechanism [20]. For these failure modes, too, the required thickness is largely independent of muscle diameter. Therefore the effect of the bladder on the force output of the actuator is generally greater when the diameter is smaller.

The presence of the bladder affects tension force in three main ways: first, it creates friction by pressing against the sleeve; second, it partially counteracts the fluid pressure by resisting expansion radially and so reducing the outward force on the sleeve which in turn reduces the axial tension in the sleeve; third, it can act as a hyperelastic spring in parallel with the actuator that applies an axial contraction force adding to the tension force in the sleeve.

Figure 2.4: Bladder failure mode.

Previous force models such as [6] and [28] have accounted for elastic energy storage in the bladder, using the Mooney-Rivlin energy function to derive a correction to the Gaylord force term. The formulation given in this section is similar in principle to those models, but makes several enhancements. First, by separately deriving the axial and circumferential stresses in the bladder, we can determine the contact pressure between the bladder and sleeve, which helps to calculate friction; it also allows us to determine the bladder's stress state when it is not inflated and not in contact with the sleeve, which impacts axial forces. Second, we apply this hyperelastic bladder model to calculate the effect of bladder pre-strain on the force curve. Lastly, we will extend the thin-walled tube bladder model into a thick-walled model to more accurately match experimental data on pre-strain.

The expression for actuator force now has four parts, as formulated in [9]: the axial tension in the sleeve strands, the outward pressure force on the ends of the muscle, the axial elastic force of the bladder, and a friction term.

$$F = F_{strands} + F_{pressure} + F_{elastic} \pm C_f P_{eff} \qquad 2.4$$

The first two terms (which act opposite each other) correspond to the ideal expression (2.3) from the potential energy model, with

$$F_{strands} = +P_{eff} * f(L) \qquad F_{pressure} = -PA_{fluid} \qquad 2.5$$

where P_{eff}, the effective pressure, is the average outward pressure exerted by the bladder on the sleeve, $f(L)$ is a function dependent on sleeve geometry to be derived below, P is the pressure of the fluid, and A_{fluid} is the cross-sectional area of the fluid inside the bladder. The difference between actual fluid pressure and the effective pressure depends on the volume, elastic properties, and strain state of the bladder. Positive force indicates tension and negative force indicates compression, so the negative $F_{pressure}$ term would be similar to compression force generated in a pneumatic cylinder, except that it is counteracted by the tension term $F_{strands}$.

Coulomb friction, the main source of hysteresis in pneumatic muscles, is proportional to the normal force between surfaces. In this case, friction surfaces exist at the intersections between strands in the sleeve, and more importantly, where the strands touch the bladder. Therefore friction, like contraction force, is proportional to the effective pressure P_{eff}. The coefficient of friction must be found empirically [21] and depends strongly on strand and bladder materials. It also can be a function of actuator length [9] because the normal force between the bladder and sleeve is the product of pressure and area, and the area of contact between them varies as the actuator length changes. The friction force is negative during the contraction stroke but positive on the extension stroke, leaving a hysteresis gap between the force curves.

The volume of rubber V_R making up the bladder is constant, since rubber is for practical purposes incompressible. It can be calculated from the inner and outer diameters $D_{RI}$and D_{RO} of the relaxed tube, and the initial length L_{R0} of the bladder before it was clamped into the sleeve:

$$V_R = \frac{\pi}{4}(D_{RO}^2 - D_{RI}^2)\, L_{R0} \qquad 2.6$$

The volume of the fluid cavity is $V_{fluid} = V - V_R = \frac{b^2 L - L^3}{4\,\pi n^2} - V_R$ and its diameter is the inner bladder diameter

$$D_{in} = \sqrt{\frac{b^2 - L^2}{n^2 \pi^2} - \frac{4}{\pi}\frac{V_R}{L}} \qquad 2.7$$

We first model the bladder as a thin-walled tube, a simplifying assumption which introduces some deviation from its real strain state but has been employed in past hyperelastic bladder models [6,28]. In this case, the circumferential stretch ratio in the rubber is approximately D_{in}/D_{RI}, which increases with the muscle diameter, and the non-linear stress-strain relationship determines the hoop stress in the bladder. Though there are numerous ways to model elastomers [29] the hyperelastic stress-strain relationship chosen here comes from the Mooney-Rivlin model of an incompressible solid due to its simplicity [30]. The strain energy density function W is

$$W = C_1(\lambda_1^2 + \lambda_2^2 + \lambda_3^2 - 3) + C_2(\lambda_1^2\lambda_2^2 + \lambda_2^2\lambda_3^2 + \lambda_3^2\lambda_1^2 - 3) \qquad 2.8$$

where C_1 and C_2 are material constants and λ_1, λ_2, λ_3 are the principal stretch ratios $\lambda_i = 1 + \varepsilon_i$ along the cylinder axis, circumference, and radius respectively:

$$\lambda_1 = L/L_{R0} \qquad 2.8a$$

$$\lambda_2 = D_{in}/D_{RI} \qquad 2.8b$$

and to maintain constant volume (incompressibility),

$$\lambda_3 = 1/(\lambda_1\lambda_2) \qquad 2.8c$$

The energy density function gives rise to the true stress relationships for a flat sheet [29],

$$\sigma_{11} - \sigma_{33} = 2\,C_1(\lambda_1^2 - \lambda_3^2) - 2\,C_2\left(\frac{1}{\lambda_1^2} - \frac{1}{\lambda_3^2}\right) \qquad 2.9a$$

$$\sigma_{22} - \sigma_{33} = 2\,C_1(\lambda_2^2 - \lambda_3^2) - 2\,C_2\left(\frac{1}{\lambda_2^2} - \frac{1}{\lambda_3^2}\right) \qquad 2.9b$$

If the bladder is very thin compared to its radius, any small section will be roughly flat and therefore obey the stress-strain relationships of equation (2.9). Previous modeling has assumed that such a wall section carries stresses only in the σ_{11} and σ_{22} axes [14]. Likewise, in this case we can take the radial true stress σ_{33} (the compressive stress through the thickness of the tube wall) to be approximately $-P$, an assumption that is necessary when treating the tube wall as a sheet. In fact, $\sigma_{33} = -P$ only at the inner wall of the tube, and $\sigma_{33} = -P_{eff}$ at the outer wall. That discrepancy will be eliminated in the thick-wall model at the end of the section.

In a thin-walled tube, the outward forces created by the pressure difference must be balanced by internal tension stress in the bladder material, at the cut shown in Figure 5.

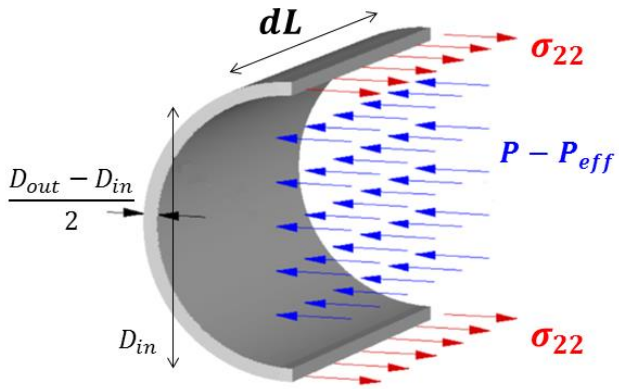

Figure 2.5: Calculation of hoop stress in the bladder.

The circumferential force in a segment *dL* of the tube is proportional to the difference between internal and external pressure times the area on which it acts:

$$2 * dF_{circ} = \left(P - P_{eff}\right) D_{in} dL \tag{2.10}$$

where D_{in} is the diameter of the fluid cavity inside the bladder, which varies with actuator length. Consequently, dividing that force by the rectangular cross-section of rubber that supports it, the average true hoop stress in the rubber is

$$\sigma_{22} = \frac{dF_{circ}}{\frac{1}{2}(D_{out} - D_{in})dL} = \frac{\left(P - P_{eff}\right) D_{in}}{\lambda_3 (D_{RO} - D_{RI})}. \tag{2.11}$$

Since the hoop stress σ_{22} depends on D_{in} and *L* as shown by substituting (2.8a,b,c) into (2.9b), we may calculate P_{eff} as a function of hoop stress and diameter and so, indirectly, of length alone:

$$P_{eff} = P - \frac{\sigma_{22} \lambda_3 (D_{RO} - D_{RI})}{D_{in}} \tag{2.12}$$

The effective pressure P_{eff} should also be constrained to non-negative values, since the bladder cannot pull inward on the sleeve. The outward pressure is balanced by the tension in the helical strands. Because they lie at an angle to the cylinder axis, their tension forces F_{strand} have both axial and circumferential components F_A and F_C. The circumferential component must counteract the pressure forces perpendicular to the muscle axis, so we treat the sleeve, too, as a thin-walled pressure vessel. Cutting a cross-section of the cylinder axially along the center line, the perpendicular force from the bladder is

$$F_{\perp} = P_{eff} D L \tag{2.13}$$

and if there are *m* strands that each wind around the cylinder *n* times, then there are $2mn$ places where strands cross the cut so that the circumferential component of force along each is

$$F_C = \frac{P_{eff} DL}{2mn} = F_{strand} \sin\theta \tag{2.14}$$

The strand force in the direction of the cylinder axis is

$$F_A = F_{strand} \cos\theta = \frac{F_C}{\tan\theta} \tag{2.15}$$

and returning to equation (2.5) we can see that:

$$F_{strands} + F_{pressure} = mF_A - PA_{fluid} = \frac{P_{eff} DL}{2n \tan\theta} - P\frac{V_{fluid}}{L}$$
$$= \frac{P_{eff} L^2}{2\pi n^2} - P\left(\frac{b^2 - L^2}{4\pi n^2} - \frac{V_R}{L}\right) \tag{2.16}$$

In the ideal case where $V_R = 0$ and $P_{eff} = P$, equation (2.16) would reduce to equation (2.3). The final contribution to the actuator force is the axial tension in the bladder, similar to a spring in parallel with the muscle. We now use the stress relationship (2.9a) for σ_{11} and find the cross-sectional area of the bladder to get

$$F_{elastic} = \sigma_{11} A_R = \frac{\sigma_{11} V_R}{L} \tag{2.17}$$

where once again we take $\sigma_{33} = -P$. The elastic force therefore depends on the diameter and length of the bladder, which when the bladder is inflated depend only on muscle length. However, in low-pressure cases where $P_{eff} = 0$, the bladder loses contact with the sleeve and it is necessary to change the definition (2.7) of D_{in} because the geometric constraint on the bladder diameter disappears. Instead we must find the bladder diameter by balancing hoop stress with internal pressure. If we set $P_{eff} = 0$ in (2.12), with $\lambda_1 = L/L_{RO}$ known and $D_{in} = \lambda_2 D_{RI}$ we can solve numerically for λ_2:

$$P\left(\lambda_3 + \frac{\lambda_2 D_{RI}}{D_{RO} - D_{RI}}\right) = 2\,C_1\left(\frac{\lambda_2}{\lambda_1} - \frac{1}{\lambda_1^3 \lambda_2^3}\right) - 2\,C_2\left(\frac{1}{\lambda_1 \lambda_2^3} - \lambda_1 \lambda_2\right) \tag{2.18}$$

The importance of this elaboration is that an inflated bladder (with a large D_{in} and λ_2) causes higher σ_{11} and more axial tension $F_{elastic}$ than the same bladder with no pressure. It therefore increases actuator force during the pressurized power stroke but not during the unpressurized return stroke. This effect is further enhanced by pre-straining the bladder, as we will see in the simulated force curves below. The numerical solution here necessitates computational methods, but given the complexity of the analytical expressions in [6] and [28] computer simulation is already the only practical way to evaluate the predictions of a force model that includes hyperelastic behavior.

The total force in this detailed model depends not only on pressure and length, but on the material properties and size of the rubber bladder. Figure 6 plots the extension and contraction force curves for a typical geometry and pressure, normalized for comparison to Figure 2.3. Force is normalized by the nominal maximum force as calculated in Eq. (2.3). The length is normalized by strand length b, and it cannot reach unity because the bladder volume prevents the sleeve diameter from approaching zero. Calculating maximum length explicitly is not necessary because as length increases past the unstretched length and diameter decreases, radial compression of the bladder and sleeve cause the strand tension to rise asymptotically. Although the exact shape of the curve depends on the pressure and the bladder thickness, several qualitative differences from Figure 2.3 persist. The nonlinearity is more pronounced, the actuator force is reduced throughout the linear portion, and the zero-force intercept occurs at a greater actuator length so that the stroke length is shorter—especially on the contraction stroke (lower curve), which is usually more important to the application.

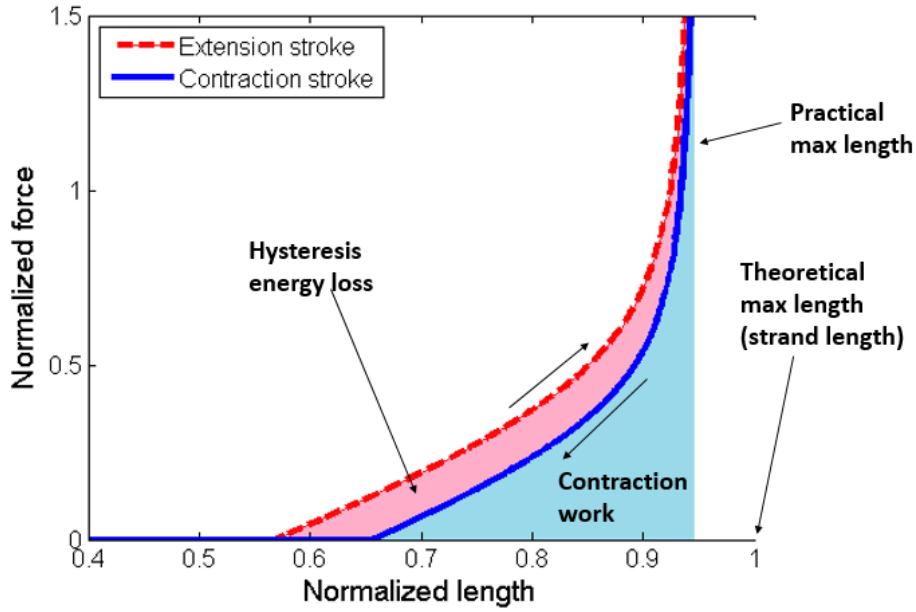

Figure 2.6: Normalized force versus length, thin-walled bladder model. Length is normalized by the strand length *b*.

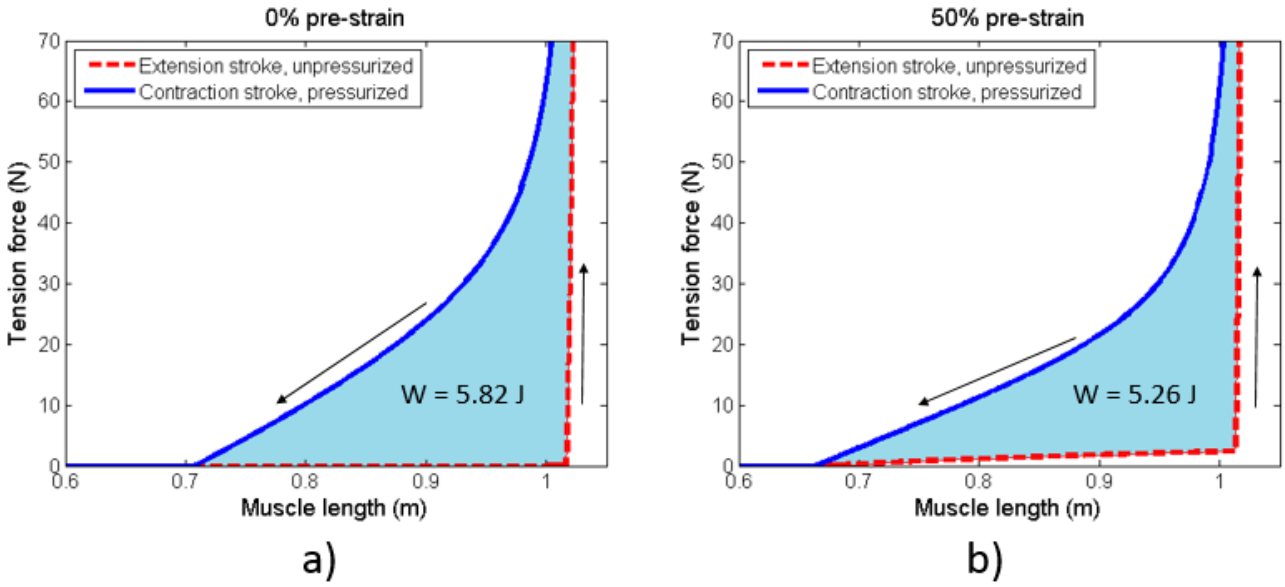

Figure 2.7: Thin-wall model of full actuation cycle with a) 0% pre-strain, b) 50% pre-strain.

Figures 2.7a and 2.7b show the power stroke and return stroke for two different bladder geometries. In Figure 2.7a, the unstretched bladder length is the same as the muscle length (no pre-strain). In Figure 2.7b, the unstretched bladder length is 2/3 of the muscle length (50% pre-strain). The actuator performs work during the pressurized contraction and then vents to atmospheric pressure, but extending it back to its nominal length still requires some work to overcome the elastic force of the bladder. The net work done by the muscle is the area between the two curves, calculated by integrating force with respect to contraction/extension distance on each curve separately and then subtracting the extension work (performed on the muscle) from the contraction work (performed by the muscle). In this case, the model predicts that pre-straining the bladder reduces the net work performed from 5.82 J to 5.26 J, despite increasing the stroke length. Experimental data from section 2.3 will show the opposite, an increase in work associated with pre-strain.

We have remedied the qualitative discrepancy by extending this force-balance model to describe the bladder as a thick-walled tube, or equivalently as some number γ of nested tubes (layers), each following the thin-wall behavior of Eqs. (2.12) and (2.17). Neglecting shear stress, their contributions to axial force (2.17) simply add. Equation (2.12) describes the pressure on the outside of each layer relative to the pressure inside, which is the outside pressure of the previous layer. Therefore the overall effective pressure is

$$P_{eff} = P - \sum_{i=0}^{\gamma} \frac{\sigma_{22_i} \lambda_{3_i} \Delta D}{\lambda_{2_i} D_{0_i}} \qquad 2.19$$

where $\Delta D = (D_{RO} - D_{RI})/\gamma$ is the difference in unstretched diameter between adjacent layers, and $D_{0_i} = D_{RI} + i\Delta D$ is the unstretched diameter of layer i. Although λ_1 is the same for all the

layers, and $\lambda_{3_i} = 1/(\lambda_1\lambda_{2_i})$ as before, λ_{2_i} now depends on both the muscle diameter D and the unstretched diameter D_{0_i} of layer i:

$$\lambda_{2_i} = \frac{D_i}{D_{0_i}} = \sqrt{\left(\frac{D}{D_{RO}}\right)^2 \left(\frac{D_{RO}}{D_{0_i}}\right)^2 + \frac{1}{\lambda_1}\left(1 - \left(\frac{D_{RO}}{D_{0_i}}\right)^2\right)} \qquad 2.20$$

Knowing λ_{2_i}, σ_{22_i} and σ_{11_i} can be found from (2.10), with $\sigma_{33_i} = P_{eff_{i-1}} = P - \sum_{j=0}^{i} \frac{\sigma_{22_j}\lambda_{3_j}\Delta D}{\lambda_{2_j} D_{0_j}}$ so that the outside pressure of each layer must be calculated sequentially.

The thick-walled model requires somewhat more computation, but improves the accuracy considerably with regard to pre-strain. Figure 2.8 shows the actuation curves and work output for various ratios of bladder length to muscle length, using the thick-walled bladder model.

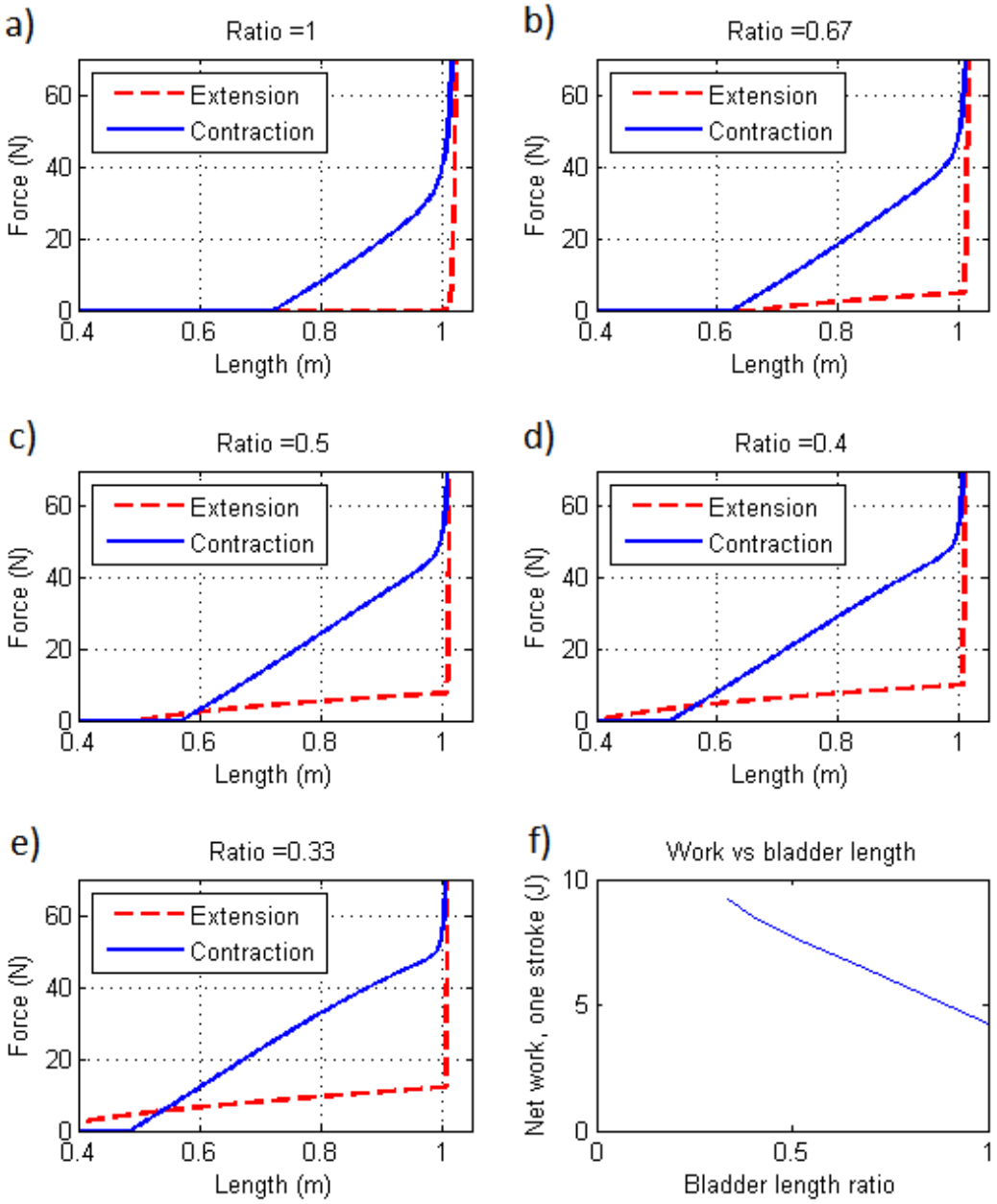

Figure 2.8: Thick-walled model of actuation curves for five different bladder lengths ranging from muscle length to 1/3 of muscle length. f) shows the net work (area between the curves) for the five cases as a function of bladder length.

The results indicate that more pre-strain (a smaller bladder length ratio) increases the net work performed by a stroke of the actuator. However, the model does not apply well to very short bladder lengths (more than 100% pre-strain), since the Mooney-Rivlin strain energy function is generally only accurate when the values of λ_1, λ_2, and λ_3 are small [31]. Therefore this model is unable to find a specific optimal level of pre-strain that maximizes the net work. Section 2.4 will compare these results to experimental data.

2.3 Muscle Testing

2.3.1 Experimental Setup

We constructed four pneumatic muscles for testing, three to examine variations in bladder pre-strain and one to examine the effects of bladder thickness and diameter. Table 2.1 shows the dimensions of each completed muscle.

Table 2.1: Geometric parameters of test muscles

Muscle	Length (mm)	Bladder length (mm)	Length ratio, pre-strain	Bladder inner diameter (mm)	Bladder thickness (mm)	Sleeve thickness (mm)	Strand length b (mm)	Turns n
A	103.25	100.5	0.97 3%	1.60	1.60	0.36	111.3	3.74
B	108.8	71.5	0.66 52%	1.60	1.60	0.36	116.0	3.87
C	98.9	54.1	0.55 82%	1.60	1.60	0.36	105.1	3.40
D	135.8	133.6	0.98 2%	3.80	0.25	0.36	142.3	4.53

The bladder thickness and inner diameter were measured with calipers to a precision of 0.05 mm. Values of b and n were determined by measuring the axial distance covered by one loop of the helix at a known diameter, when the muscle is stretched fully. For a given weave of sleeve material, the ratio b/n is constant—in this case, about 30 mm. Higher values of b/n, which correspond to increased sleeve diameter during contraction, increase the

actuator force according to Eq. (2.3). All bladders were natural latex rubber, which has better fatigue life than synthetics [19].

We performed several tensile tests at different pressures on each muscle. Pressure was held constant during each test, and starting from the zero-tension position the length was gradually increased by applying tension to the ends with a winch until the muscle reached its fully stretched length. The length was then decreased again until the tension force reached zero for the contraction stroke. Length was measured with an SLS190 linear potentiometer and tension force with a Transducer Techniques SSM-200 load cell. For muscles A, B, and C, test pressures ranged from 0 to 690 kPa (0 to 100 psi). For muscle D, the highest pressure tested was 345 kPa (50 psi) because the bladder failed during that test.

To determine the stiffness of the bladder materials, we performed uniaxial tensile tests on a sample of each thickness, and compared the results to the Mooney-Rivlin stress equation to choose the C_1 and C_2 material constants.

2.3.2 Results

Figure 2.9 gives the results of the uniaxial tensile tests for the bladder materials, along with the Mooney-Rivlin stress values for the same stretch range. The Mooney-Rivlin constants are the average experimental values from [32]. Finding new Mooney-Rivlin constants for each tube sample would require biaxial or compression testing [33], so those values from the literature are used throughout these results.

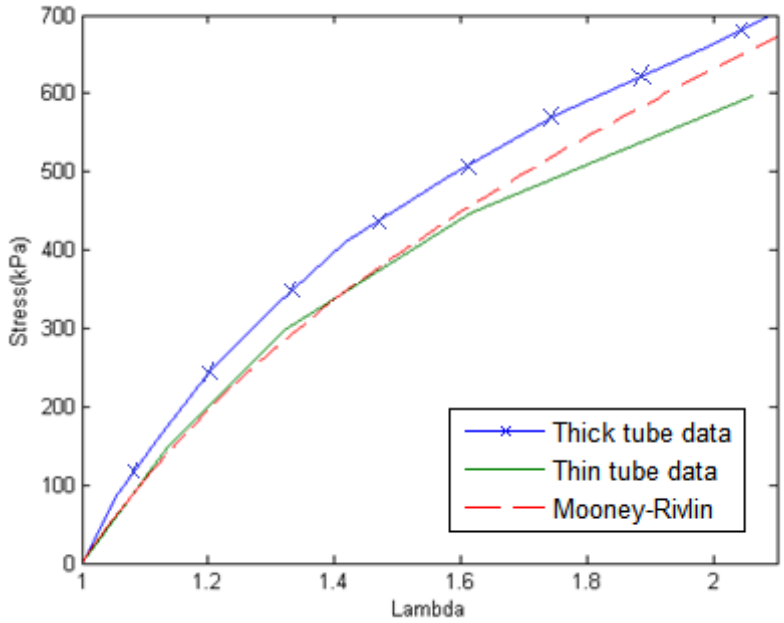

Figure 2.9: Bladder tensile test results. Thick tube data is from the bladder type used for muscles A, B, and C. Thin tube bladder was used for muscle D. The Mooney-Rivlin curve shows theoretical stress from a uniaxial Mooney-Rivlin model with C_1 = 161 kPa, C_2 = 39 kPa [32].

Figure 2.10 shows tensile test results for each of the four muscles, both unpressurized and pressurized. The unpressurized force curves reflect stretching of the sleeves and connectors as the muscles approach their maximum lengths at the right side of each graph. The unpressurized curves for the pre-strained muscles (B and C) stay above zero over much of the length range shown, because of elastic contraction force of the bladder. The pre-straining also raises the high-pressure force curves for B and C above that of A. Note that the pressure value for muscle D is only about 53% of the values for A, B, and C, but because of

the thinner bladder material and larger bladder diameter, it achieves almost as much contraction force. Its hysteresis is lower because friction is proportional to effective pressure.

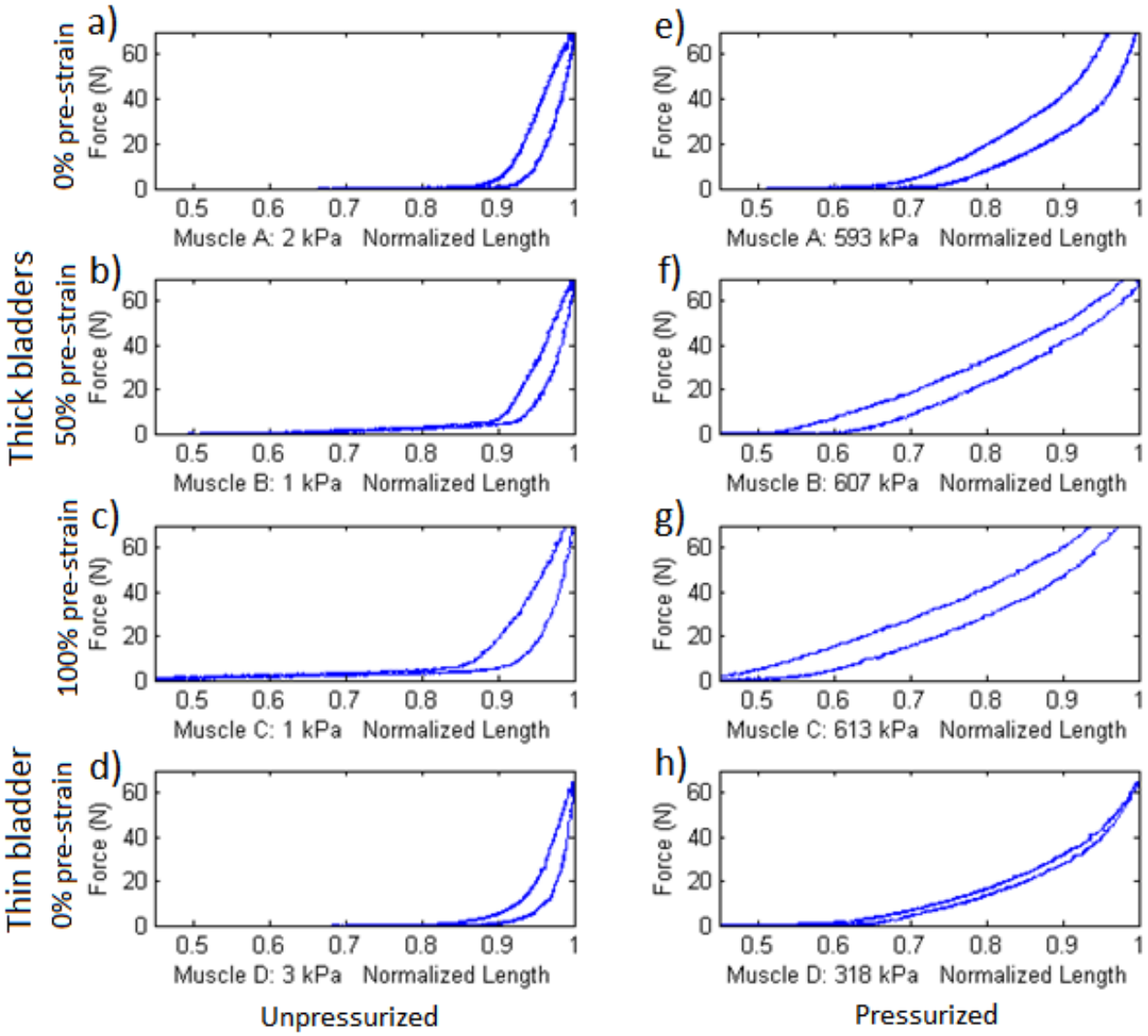

Figure 2.10: Selected data from tensile tests of the four test muscles A, B, C, and D. Lengths are normalized by stretched muscle length, not strand length. a)-d): unpressurized. e)-h) pressurized.

2.4 Comparison with Model Predictions

Figures 2.11-2.14 compare experimental results for each muscle with the predictions of the thick-walled bladder model for that muscle's geometry. The model captures key features of most of the data sets, especially the increase in total work associated with pre-strain in muscles B and C, on which the thin-walled model fails.

A series linear spring representing connector stretch at the ends has been added to the model. This addition is necessary because the attachment points between the actuator and test apparatus consisted of a loop of nylon monofilament which is thick enough to have some small resistance to bending and acts as a tension spring with a low spring constant; therefore when tension forces are small it causes the measured length of the actuator to be less than the actual length by an amount equal to the contraction of the connector. This was an error in experimental design but can be rectified by subtracting a correction term $F/k_{connector}$ from the predicted length to account for the connector contraction. The linear spring constant is calibrated to match the zero-pressure data in order to ensure that it reflects passive stretching of the connectors rather than changing the behavior of the model with respect to actuator contraction.

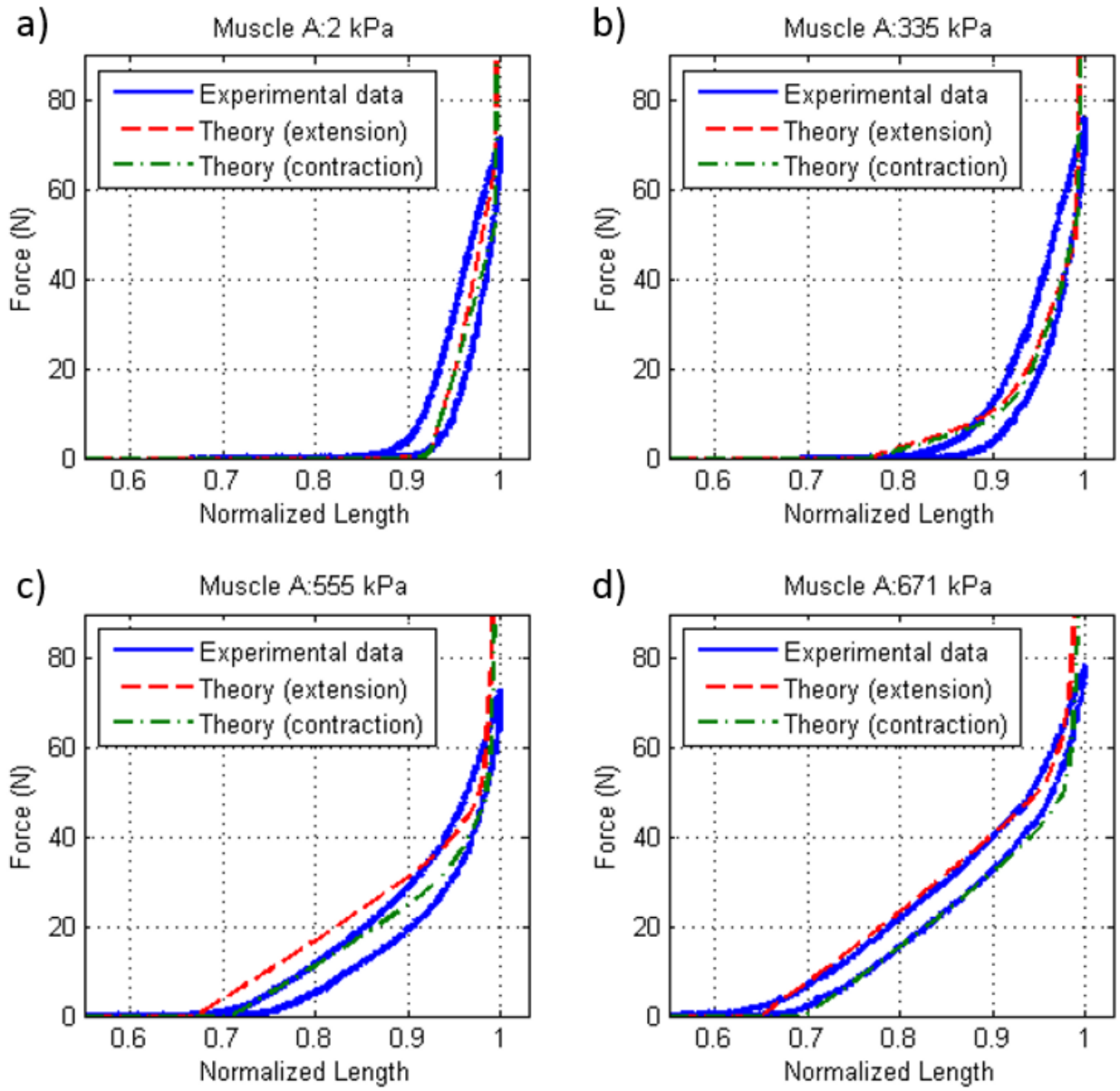

Figure 2.11: Thick-walled model compared to data for muscle A, thick bladder with 3% pre-strain.

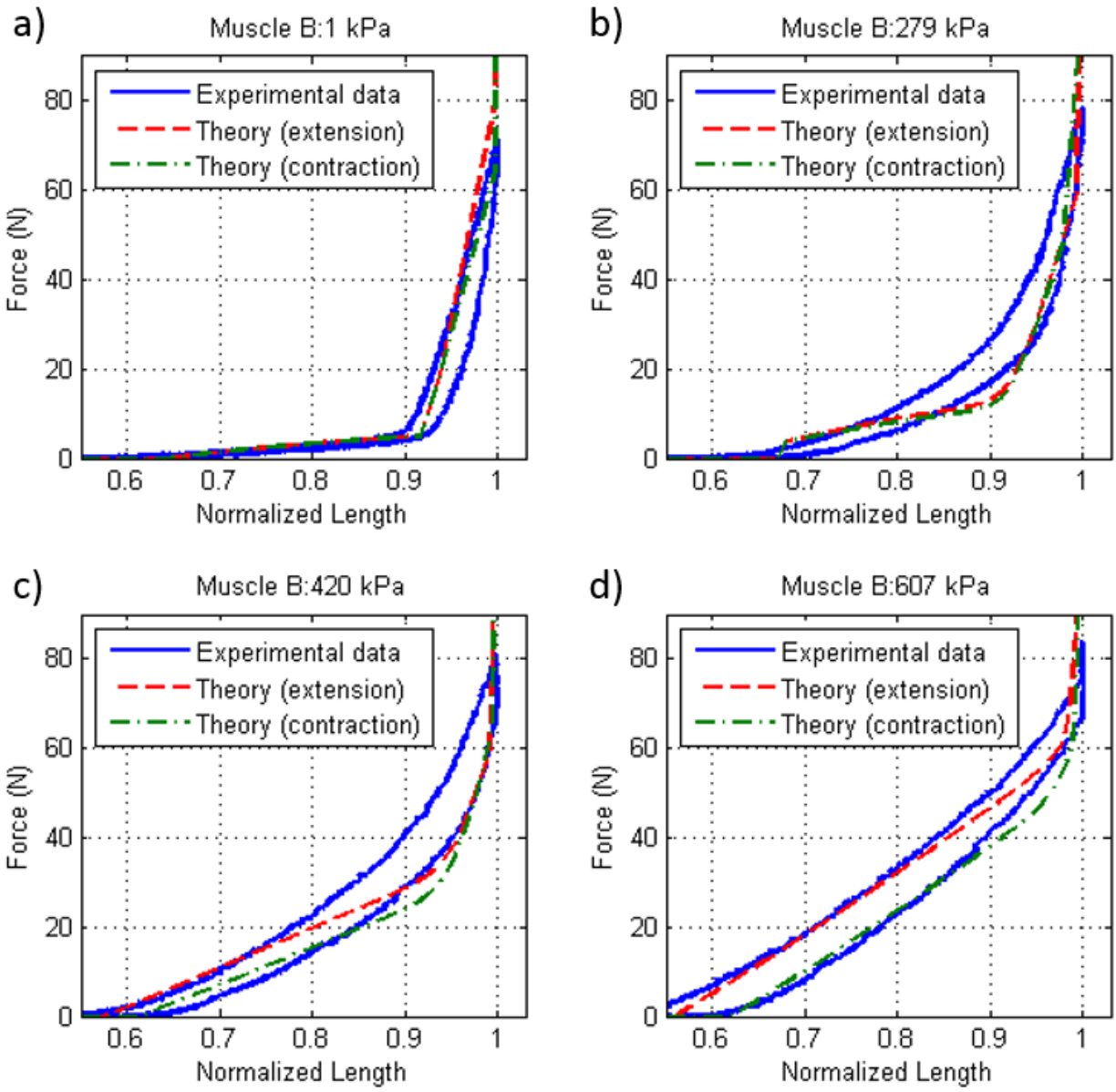

Figure 2.12: Thick-walled model compared to data for muscle B, thick bladder with 52% pre-strain.

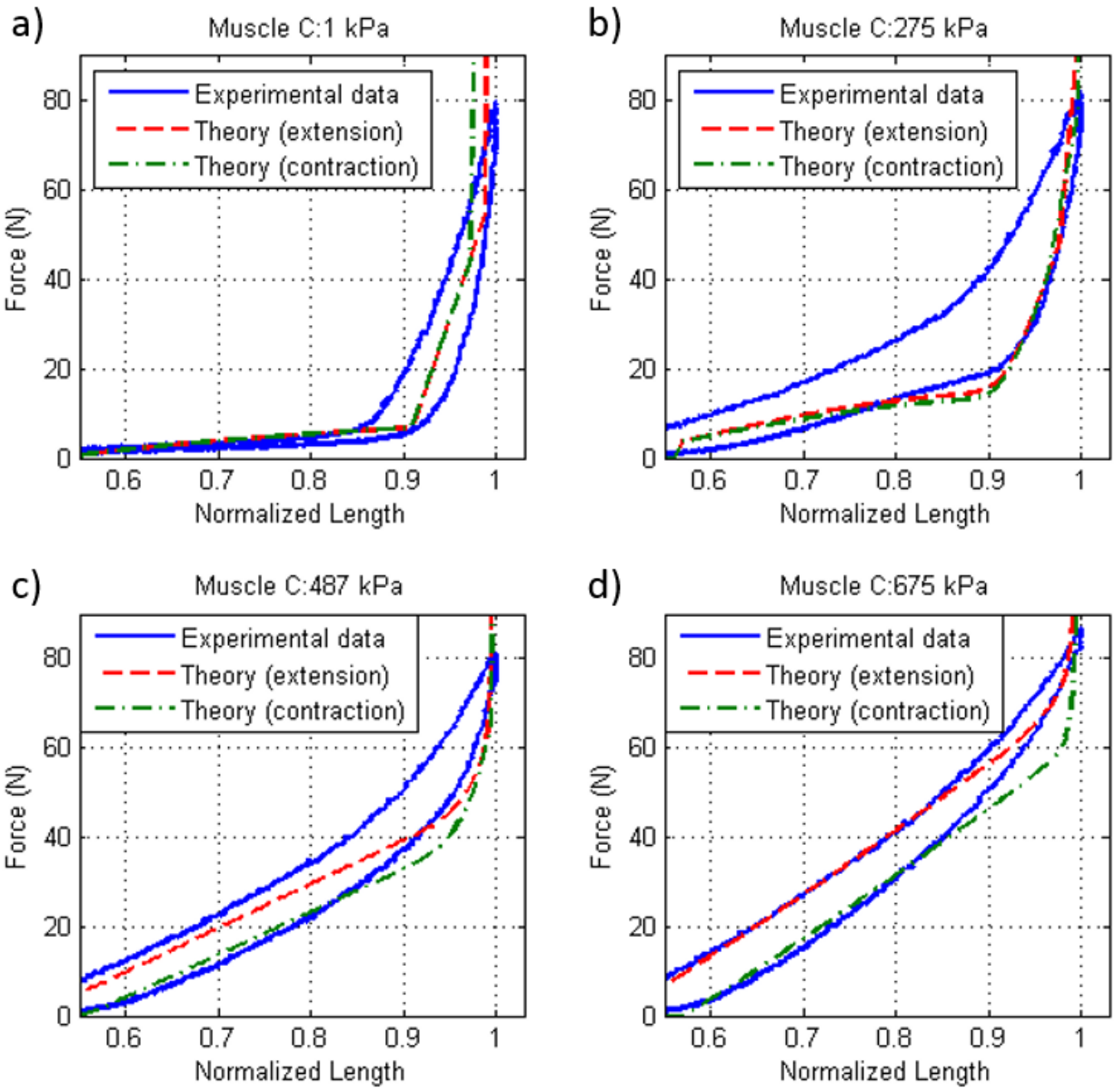

Figure 2.13: Thick-walled model compared to data for muscle C, thick bladder with 82% pre-strain.

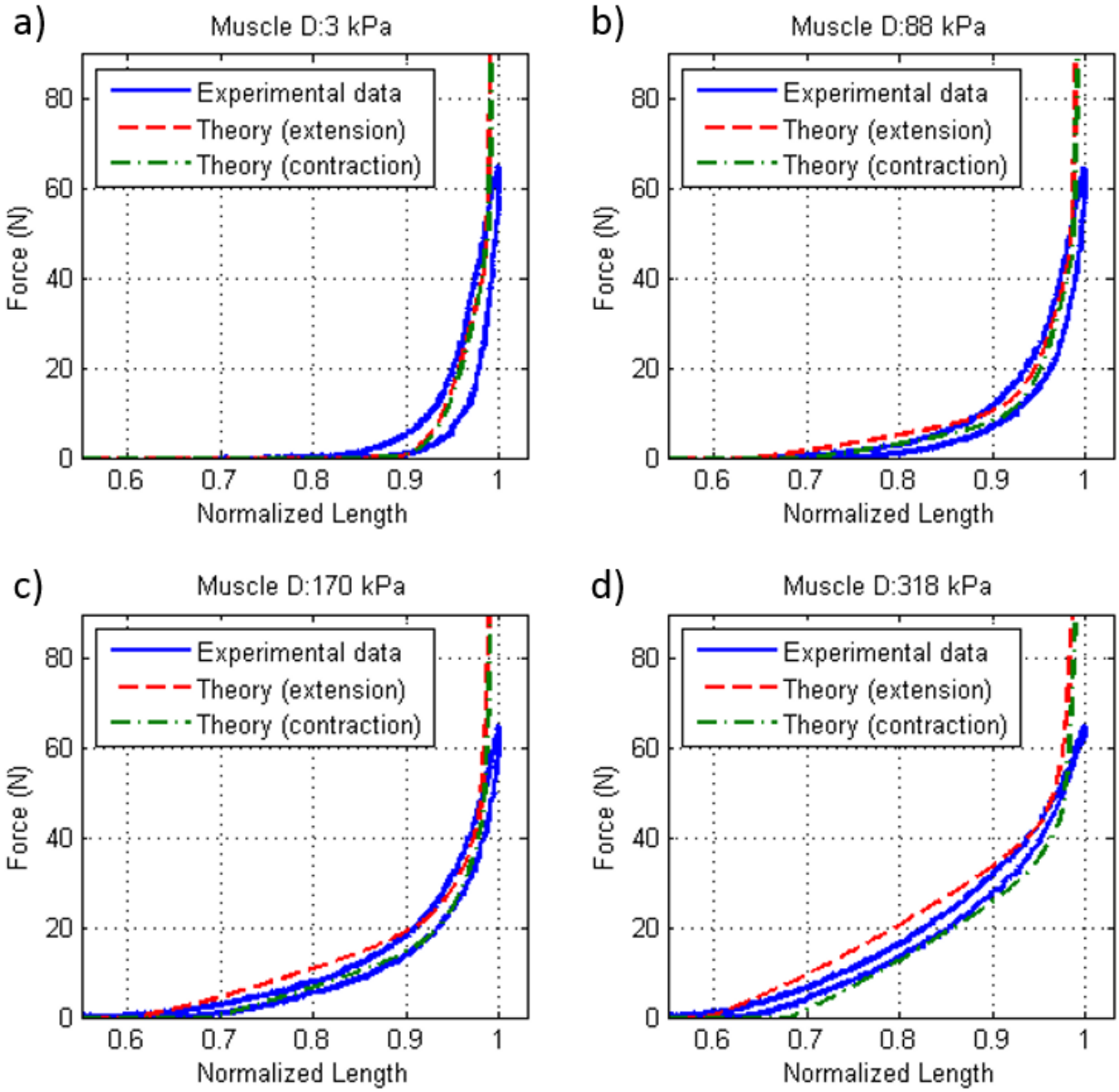

Figure 2.14: Thick-walled model compared to data for muscle D, thin bladder with 2% pre-strain.

Muscle A fits the model well at low pressure and high pressure, but at intermediate pressures the model predicts more total contraction than the data show. This may result from errors in the constants describing the bladder material that affect the threshold pressure.

Muscle B has similar problems, though less pronounced. For muscle C, the contraction curves fit well but the hysteresis prediction fails completely, resulting in much higher-than-predicted forces during extension. Hysteresis seems to vary widely from test to test, and to be not always proportional to effective pressure. In contrast, muscle D fits the predictions quite well, partly because of its low hysteresis. Here the thick-walled model is unnecessary and gives similar results to the thin-walled model, because the bladder's thickness is in fact much less than its diameter.

Numerous other complicating factors contribute to inaccuracy in this model. The clamps that bind the bladder to the ends of the sleeve cause the shape to be non-cylindrical at the ends, which reduces the volume of fluid that can be held inside, especially in short muscles with large diameters [25]. Non-zero sleeve thickness reduces the internal volume. Sleeve strands may stretch under high tension, and more importantly, they resist the bending associated with contraction [28]. Besides simple friction, hysteresis may result from plastic deformation in the sleeve or connectors, clamps sliding along the outside of the sleeve, stress relaxation of the bladder [30], and energy dissipation in the fluid flow. Many of these can be ignored in muscle design for static forces because the force curve can be predicted accurately enough from geometric and material parameters. Work on small-diameter pneumatic muscles has shown that the non-cylindrical end effects are not significant because the rounded portion is relatively small, but in larger diameter or very short muscles it becomes substantial [26]. Detailed results exist that show the effects of valve flow in dynamic actuator systems [34]. Better modeling of actuator hysteresis, however, is important for practical use, especially where actuators are used in antagonistic pairs and must overcome each other's extension forces in addition to the actual load.

The nonlinear elasticity of the bladder, in typical tube geometries, causes a discontinuity in the pressure-diameter relationship and allows inflation to occur suddenly and dramatically above a certain pressure, an effect often observed when inflating cylindrical balloons. Above this threshold pressure (the pressure at which the bladder would inflate if unconstrained by the sleeve) the bladder begins to apply substantial outward force to the sleeve and therefore generate axial force. Threshold pressure depends on bladder thickness, diameter, and modulus. For this reason the thin and large-diameter bladder of muscle D lets it achieve much higher actuator forces for a given pressure, which reduces the energy input needed; it also reduces the maximum actuator force (compared to muscle C, for instance) because the bladder cannot withstand high pressures and cannot contribute significant axial elastic force. Fatigue life may also be compromised by a thin bladder.

Muscles A, B, and C are similar except for the degree of pre-strain, and clearly show that more pre-strain equates to higher actuator force, longer stroke length, and more work performed in a single stroke. The work required to extend the unpressurized muscle on the return stroke also increases, but not enough to offset the increase in contraction force. Pre-strain does not appear to have a significant effect on the threshold pressure.

2.5. CONCLUSIONS

The model presented here allows prediction of McKibben muscle force curves with sufficient accuracy to allow optimization of sleeve geometry, bladder diameter and thickness, and bladder material. The thick-walled version of the model can also predict the effects of bladder pre-strain. This factor is particularly important for small-scale McKibben muscles where bladder thickness is often a large proportion of muscle diameter and has an outsize effect on threshold pressure and contraction force. Our results show that when chosen

appropriately, bladder pre-strain can increase both the force and the net work performed during a stroke of the actuator at the expense of higher unpressurized force.

Engineers engaged in designing McKibben muscles for a particular application can benefit from this model when the requirements include specific force levels at specific contraction lengths (as when designing for a desired torque on a joint), total stroke length above a given force level (for instance, the need to lift a static load a certain distance), or maximizing work performed in one stroke. It minimizes the trial and error required for the process of choosing actuator parameters by allowing the engineer to evaluate the predicted quasi-static behavior of numerous hypothetical actuator geometries simultaneously. By specifying the force-length relationship more accurately, the model also lends itself to the design of non-circular cams that vary in radius to control their torque throughout the stroke and thereby utilize all the available contraction energy. Applications that depend on detailed understand of how actuator force varies with contraction can rely on this model to find a set of geometric parameters for the muscle (and especially for the bladder) that will provide the required outputs at the appropriate pressure, and to evaluate trade-offs between the high energy efficiency associated with thin bladder and the greater forces associated with thick bladders and high levels of pre-strain.

We hope that analysis of this type will help to make the use of McKibben muscles practical for commonplace engineered systems that require a lightweight, simple, inexpensive, and reliable actuator without the need for drawn-out development and testing.

REFERENCES

[1] “More Help for Polio Victims,” 1958, The Buckingham Post, Originally from Newsweek, 21 March 1958. http://cyberneticzoo.com/bionics/1957-artificial-muscle-joseph-laws-mckibben-american/

[2] Tondu, B., 2012, “Modelling of the McKibben artificial muscle: A review,” J. Intelligent Material Systems and Structures, 23(3), pp. 225-253.

[3] Gaiser, I., Wiegand, R., Ivlev, O., Andres, A., Breitwieser, H., Schulz, S., and Bretthauer, G., 2012, *Compliant Robotics and Automation with Flexible Fluidic Actuators and Inflatable Structures*. G. Berselli (Ed.), Smart Actuation and Sensing Systems - Recent Advances and Future Challenges. InTech.

[4] Tondu, B. and Lopez, P., 2000, “Modeling and control of McKibben artificial muscle robot actuators,” IEEE Control Systems, 20, pp. 15-38.

[5] Klute, G., Czerniecki, J., and Hannaford, B., 2002, “Artificial muscles: Actuators for biorobotic systems,” Intl. J. Robotics Research, 21, pp. 295-309.

[6] Klute, G. K. and Hannaford, B., 2000 “Accounting for Elastic Energy Storage in McKibben Artificial Muscle Actuators,” ASME J. Dynamic Systems, Measurement, and Control, 122(2), pp. 386-388.

[7] Gaylord, R. H., 1958, “Fluid actuated motor system and stroking device,” United States Patent 2,844,126.

[8] Shulte, H.F., 1961, “The characteristics of the McKibben artificial muscle,” *The application of external power in prosthetics and orthotics*, 874, pp. 94-115.

[9] Schulte, H.F., Adamski, D.F., and Pearson, J.R., 1961, "Characteristics of the Braided Fluid Actuator," Technical Report No. 5, The University of Michigan Medical School Department of Physical Medicine and Rehabilitation Orthetics Research Project.

[10] Daerden, F. and Lefeber, D., 2000, "Pneumatic artificial muscles: actuators for robotics and automation," European J. Mechanical and Environmental Engineering, 47, pp. 10-21.

[11] Marcinčin, J., and Palko, A., 1993, "Negative pressure artificial muscle—An unconventional drive of robotic and handling systems," Riecansky Science Publishing Co., Slovak Republic pp. 350-354.

[12] Yee, N., and Coghill, G., 2002, "Modelling of a novel rotary pneumatic muscle," Proc. Australasian Conf. Robotics and Automation pp. 186-190.

[13] Baldwin, H. A., 1967, "Realizable models of muscle function," Proc. First Rock Biomechanics Symposium pp. 139-148.

[14] Daerden, F., 1999, "Conception and realization of pleated pneumatic artificial muscles and their use as compliant actuation elements", Ph.D, Thesis, Vrije Universiteit Brussel, Belgium.

[15] Ranjan, R., Upadhyay, P., Kumar, A., and Dhyani, P., 2012, "Theoretical and experimental modeling of air muscle," Intl. J. Emerging Technology and Advanced Engineering, 2, pp. 112-119.

[16] Schroder, J., Erol, D., Kawamura, K., and Dillman, R., 2003 "Dynamic pneumatic actuator model for a model-based torque controller," IEEE Intl. Symp. Computational Intelligence in Robotics and Automation (CIRA), 1, pp. 342-347.

[17] Schroder, J., Kawamura, K., Gockel, T., and Dillmann, R., 2003 "Improved control of a humanoid arm driven by pneumatic actuators," Proc. Third IEEE International Conference on Humanoid Robots.

[18] Chou, C.P. and Hannaford, B., 1996 “Measurement and Modeling of McKibben Pneumatic Artificial Muscles,” IEEE Trans. Robotics and Automation, 12(1), pp. 90-102.

[19] Klute, G. K. and Hannaford, B., 1998 “Fatigue Characteristics of McKibben Artificial Muscle Actuators,” Proc. IEEE/RSJ Int. Conf. on Intelligent Robots and Systems Innovations in Theory Practice and Applications, 98(36), pp. 190.

[20] Woods, B., Gentry, M., Kothera, C., and Wereley, N., 2012 “Fatigue life testing of swaged pneumatic artificial muscles as actuators for aerospace applications,” J. Intelligent Material Systems and Structures, 23-3, pp. 327-343.

[21] Tondu, B., 2012, “Modelling of the McKibben artificial muscle: A review,” J. Intelligent Material Systems and Structures, 23(3), pp. 225-253.

[22] Davis, S., Tsagarakis, N., Canderle, J., and Caldwell, D., 2003, “Enhanced modelling and performance in braided pneumatic muscle actuators,” Intl. J. Robotics Research, 22, pp. 213-227.

[23] Ito, A., Kiyoto, K., and Furuya, N., 2010, “Motion control of parallel manipulator using pneumatic artificial actuators,” Proc. IEEE, Intl. Conf. Robotics and Biomimetics pp. 460-465.

[24] Sugimoto, Y., Naniwa, K., and Osuka, K., 2010, “Stability analysis of robot motions driven by McKibben pneumatic actuator,” Intl. Conf. Intelligent Robots and Systems, 2010, pp. 3049-3054.

[25] Tiwari, R., Meller, M. A., Wajcs, K. B., Moses, C., Reveles, I., and Garcia, E., 2012, “Hydraulic artificial muscles,” J. of Intelligent Material Systems and Structures, 23, pp. 301-312.

[26] Hocking, E., and Wereley, N., 2013 “Analysis of nonlinear elastic behavior in miniature pneumatic artificial muscles,” Smart Materials and Structures 22-014016.

[27] Ball, E., Lin, Y., and Garcia, E., 2013 “Characterization and modeling of geometric variations in McKibben pneumatic artificial muscles,” Proc. SPIE 8686-05.

[28] Kothera, C.S., Jangid, M., Sirohi, J., and Wereley, N.M., 2009, “Experimental Characterization and Static Modeling of McKibben Actuators,” *J. Mech. Des.* 131(9), 091010.

[29] Beda, T., 2007, “Modeling hyperelastic behavior of rubber: A novel invariant-based and a review of constitutive models,” J. Polymer Science Part B: Polymer Physics, 45(13), pp. 1713-1732.

[30] Niemczura, J. G., 2010, “On the Response of Rubbers at High Strain Rates,” Sandia National Laboratories Report, SAND2010-1480 Ch. 2.3.

[31] Finney, R. H., 2001, “Finite Element Analysis,” *Engineering With Rubber*, Hanser, pp. 266-267.

[32] Aernouts, J., Couckuyt, I., Crombecq, K., and Dirckx, J., 2010, “Elastic characterization of membranes with a complex shape using point indentation measurements and inverse modeling,” Intl. J. Engineering Science, 48(6), pp. 599-611.

[33] Feng, W. W., and Hallquist, J. O., 2012, “On Mooney-Rivlin Constants for Elastomers,” Proc. LS-DYNA Users Conference 12.

[34] Kang, B. S., Kothera, C. S., Woods, B. K. S., and Wereley, N. M., 2009, “Dynamic modeling of Mckibben pneumatic artificial muscles for antagonistic actuation,” Intl. Conf. Robotics and Automation (ICRA), 12-17, pp.182-187.

CHAPTER 3

MULTIFERROIC GENERATION OF TORQUE ON A MAGNETIC DIPOLE INSIDE A NANO-RING

Abstract

We examine the micromagnetic interactions between a directionally magnetized nickel nano-ring and a nano bar magnet in the center of the ring, concluding that inclusion of the bar in the system positions and then stabilizes the magnetic state of the ring, so that subsequent application of strain can create torque between the ring and bar. Simulation using a finite element implementation of the Landau-Lifshitz-Gilbert equation demonstrates that when the ring and bar are initially magnetized in the same direction, magnetostatic repulsion between their poles causes the ring magnetization to spin 180 degrees, while the bar magnetization is fixed by shape anisotropy. The resulting state minimizes the magnetostatic energy and so is stable. Piezoelectric strain on this stabilized system causes a small rotation of the ring magnetization relative to the bar, through the magnetostrictive effect. The predicted torque in a 700 nm ring is 2.0×10^{-18} Nm. We discuss how this technique could be applied in a MEMS actuator, and compare its potential and scaling laws to an electrostatic motor.

3.1 Introduction & Background

Micro- and nano-scale electromechanical actuation has been accomplished by various means including miniaturized electromagnets, piezoelectric materials, and electrostatic forces [1-5]. The applications of such actuators include medical devices, display technologies, adaptive optics, and sensors [5-8]. However, existing actuators have limitations in scaling, frequency rectification, heat generation, voltage requirements, and power output that can

make them impractical in certain scenarios [9, 10]. Improvements in small-scale torque and power density in particular stand to greatly benefit the practicality of MEMS devices. Multiferroic technology is an emerging research area in which ferromagnetic and ferroelectric materials together can allow control of magnetism by electricity [11]. New composite multiferroic materials have potential for use in actuators because they can use low-voltage electrical inputs to alter magnetization and magnetic field at small scales (one micron or less) where traditional electromagnets cannot function. Past research has demonstrated rotation of magnetization in nano-magnets by applied electric field [12, 13].

A multiferroic actuator requires not only the ability to control magnetism electrically, but also a mechanism for translating magnetic field into torque and extracting work from it. This research addresses magnetic interactions between nano-magnet dipoles and multiferroic nano-rings, including the effects of electric field application and the resulting torque generation which has potential for developing a spinning actuator (multiferroic nano-motor) with high torque and power output.

3.1.1 Onion State Magnetization and Strain-Mediated Multiferroics

Ferromagnetic nano-rings in the absence of external fields tend to occupy two primary magnetic states. The lowest-energy (stable) configuration is the vortex state, in which magnetization at all points is parallel to the circumference (Figure 3.1a). The second, meta-stable state, known as the onion state (Figure 3.1b), is created by temporary application of an in-plane magnetic field [14]. These rings are typically 0.5 to 4 microns in diameter and 15 to 100 nm thick.

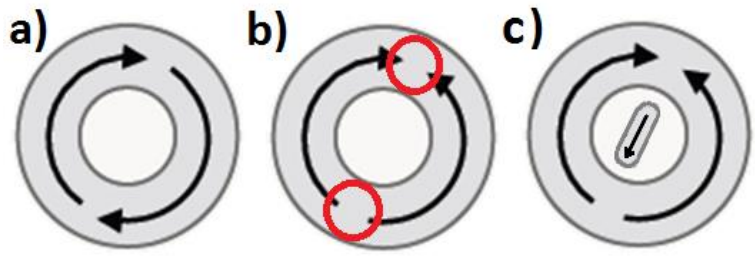

Figure 3.1: Domains in magnetic nano-rings, a) vortex state, b) onion state, with domain walls circled, and c) onion state with bar magnet.

Shape anisotropy aligns the magnetization parallel to the circumference of the ring. This means the two sides of the ring can stay magnetized with opposite chirality, resulting in two small domain walls at the boundaries between them (Figure 3.1b). The overall magnetization of the ring is along the line between these domain walls. Unlike the vortex state, stray field emanates from the domain walls and can affect its surroundings.

Research on manipulation of onion state orientation in nano-rings is ongoing [12, 15-17]. An ideal amorphous or nano-crystalline ring has no preferred orientation for the onion state, and so no energy barrier to overcome in moving the domain walls. This makes the energy cost to rotate even a non-ideal onion state low compared to other configurations with similar stray fields.

Multiferroic composites make it possible to re-orient the onion state with an electric field by coupling polarization indirectly to magnetization [18]. A magnetostrictive film is mechanically bonded to a piezoelectric film underneath it, so that anisotropic strain generated piezoelectrically is transferred to the magnetic layer [11]. In single-domain magnets the inverse magnetostrictive effect (also called the Villari effect) then creates hard and easy axes of magnetization aligned with the principle stresses, by adding a magnetostrictive energy

component to the total magnetic energy [19]. Equation 3.1 shows how the magnetostrictive energy density varies with the angle between stress and magnetization.

$$E_\sigma = \frac{3}{2}\lambda_s(\sigma_{11} - \sigma_{22})\sin^2\theta \tag{3.1}$$

Here E_σ is the contribution of strain to magnetic energy density, λ_s is the isotropic magnetostrictive coefficient of the material, a constant value which may be positive or negative, σ_{11} and σ_{22} are the in-plane principle stresses (σ_{33} is assumed to be negligible), and θ is the angle between the first principle strain direction and the direction of magnetization at the point in question. The total magnetostrictive energy of the system is found by integrating E_σ over the volume of the magnet. If both magnetization and stress are uniform throughout the magnet, the energy will be proportional to the applied stress. This magnetostrictive anisotropy tends to drive the magnetization toward alignment with the applied stress (parallel or perpendicular depending on the sign of λ_s) to reduce the magnetostrictive energy, though such motion may be resisted by shape anisotropy (if the magnet is asymmetric), external (applied) magnetic field, or magnetocrystalline anisotropy in crystalline materials. The balance between these effects will determine the equilibrium direction of magnetization.

In a single domain magnet with no overall crystal structure and no applied field, magnetostriction and shape anisotropy control the equilibrium. In symmetric onion-state rings, shape anisotropy creates no preferred axis, so stress alone can dominate the onion state orientation.

3.1.2 Magnetic Coupling into the Environment

Multiferroic actuation requires coupling the rotating magnetic field of the onion state into a MEMS/NEMS device. By analogy to traditional electric motors, the magnetic ring and piezoelectric film comprise a stator. The motor can do work by applying a torque, via magnetic field, between the stator and a rotor spinning at the desired rotation rate.

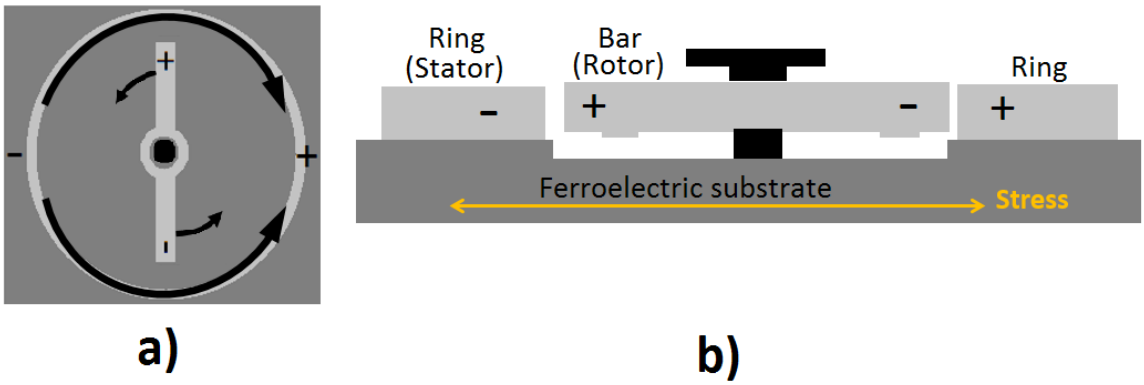

Figure 3.2: Motor configuration with bar rotor pinned at the center of the stator ring. a) top view, b) side view.

Some previous magnetic micromotors with rotors at the 1-µm to 10-µm scale have used surface tension to hold the rotor in place while an external magnetic field is applied [20, 21]. These designs have the advantage of remote actuation by a larger device that generates the field without need for electrical connections near the rotor, an advantage that could be applied more broadly if combined with nanoscale mechanical bearing technologies. Some nanomotors have used chemical energy sources with biological materials for the rotor structure and bearing [22]. Self-contained nanomotors (containing both a stator and a rotor) often use electrostatic actuation instead of magnetic, like one that used carbon nanotubes to

form the bearing [23]. Larger examples of magnetic micromotors have used a combination of magnetic levitation (for reduced friction) and a mechanical shaft [24], which it may be possible to scale down for use with a multiferroic motor. A number of piezoelectric micromotors have also been demonstrated, producing strain directly from voltages applied to the actuator; in order to produce large motions, they require complex mechanisms for frequency rectification.

Recent work proves that the onion-state stray field can capture and reposition superparamagnetic beads [13]. The attraction force between the domain wall and bead limits the torque, and also the rotation rate—if fluid drag due to the bead's rotation exceeds the magnetic force, the bead separates from the domain wall.

Alternatively, a permanent dipole bar magnet spinning in the middle of the ring (Figure 3.1c) has some advantages. It magnetically attracts both onion domain walls, doubling the coupling strength. Except for a small gap, it can form a flux closure domain to complete the magnetic circuit of the onion state, improving torque and nearly eliminating stray field. By reducing the demagnetization energy, it creates an energy well that stabilizes the onion state against perturbations that might cause it to collapse without strain. The rotor also has a fixed point at the center where a low-friction bearing and shaft could hold it in place even if magnetic coupling is broken.

3.2 Theory of Ring-Bar Interaction

The time-dependent development of micromagnetic systems such as nano-rings is governed by the Landau-Lifshitz-Gilbert equation (LLG) [25], which calculates precession and damping of dipoles taking into account demagnetizing field as well as magnetostrictive and exchange energies. Using this approach, time-dependent simulations of a nano-ring with

an appropriate geometry and a uniform initial magnetization (simulating the effect of a strong applied field quickly turned off), generally converge into an onion state in an apparently meta-stable equilibrium [13].

3.2.1 Simplified Magnetostatic Energy Minimization

LLG simulation can also predict the interaction of such a ring with a bar at its center, but a simplified analysis illustrates the mechanisms more clearly. Instead of a time-dependent solution, we account only for the magnetic "charge" (actually magnetization flux normal to the surface [19]), aggregate it into point charges, and write an expression for magnetostatic energy for the entire system as a function of the domain wall rotation. Minimizing this energy yields the equilibrium orientation of the onion state. This simplification assumes the bar cannot disturb the shape of the onion state, only its orientation. Bar magnetization is assumed uniform along its axis, because its aspect ratio is high enough that shape anisotropy keeps its magnetization aligned with its edges. Therefore, surface magnetic charges exist only at the bar ends, one positive, one negative. The magnitude of each charge is $q_{bar} = \pm t_{bar} w_{bar} M_s$, where *w* is the width of the bar, *t* its thickness, and M_s the saturation magnetization of the bar material.

The ring has magnetic charge only at the domain walls, because elsewhere its magnetization is parallel to the edges and, though not uniform, has no divergence. Approximating the domain walls as point charges, the contributions of the two halves of the onion state add: $q_{ring} = \pm 2 t_{ring} w_{ring} M_s$, where w_{ring} is the difference between the inner and outer radii. If Ψ_{ij} is the magnetic scalar potential due to point charge *j* at point *i* [26], then the magnetostatic energy of this system is

$$U_m = \frac{1}{2}\sum_{i,j} q_i \Psi_{ij} \qquad \Psi_{ij} = \frac{\mu_0 q_j}{4\,\pi r_{ij}} \tag{3.2}$$

For these four point charges, an offset angle β between the orientations of the bar and the onion state gives rise to a magnetostatic energy that is minimized when they align, with the negative end of the bar closest to the positive domain wall on the ring ($\beta = 0$).

3.2.2 Predicted Torque

The alignment and strong coupling between a stator ring and a dipole rotor permit multiferroic torque generation. Stress applied to the ring rotates the onion state toward the principal stress, away from its alignment with the rotor. The torque between them depends on the offset angle β. It is the derivative of the magnetostatic energy in equation 3.2, $\tau_{bar} = dU_m/d\beta$.

The interaction of the two ring poles is neglected because it does not vary, and likewise for the two poles of the bar. If the Euclidean distance between the positive bar pole and the negative ring pole (a function of β) is *A*, and the distance from the positive ring pole to the positive bar pole is *B*, then the variable portion of magnetostatic energy is

$$U_{m_{var}} = 2\frac{\mu_0}{4\pi} q_{ring} q_{bar} \left(\frac{1}{B} - \frac{1}{A}\right) \tag{3.3}$$

Taking the derivative and applying it to the ring and bar geometry in Table 3.1, we find the torque curve in Figure 3.3a, and a maximum torque value of about 2.1×10^{-18} Nm.

If strain is high, magnetostriction dominates, overwhelming the coupling between ring and bar and causing the onion state to rotate far out of alignment, (right half of Figure 3.3a). If the strain or magnetostrictive coefficient is small, the onion state maintains alignment to the bar, but with a small deflection. Maximum torque occurs at an intermediate point where the

small gap in the magnetic circuit allows strong coupling but the misalignment is enough to direct forces circumferentially instead of just radially. To reach it, stress must be adjusted until the strengths of the magnetostriction and the magnetic attraction match. Torque generated by a given stress is determined by adding the integral for magnetostrictive energy in equation 3.1 [19] to the energy in equation 3.3 to obtain an expression for total energy of the system:

$$U_{total} = U_m + U_\sigma = \frac{1}{2}\sum_{i,j} q_i \Psi_{ij} + \frac{3}{2}\lambda_s \int_{ring} (\sigma_{11} - \sigma_{22}) \sin^2\theta \qquad 3.4$$

Stress is assumed constant throughout the ring. Only θ, the angle between magnetization and strain, varies. In the integral, each segment of ring besides the domain walls cancels out an opposing segment. The magnetization of a transverse domain wall points in the direction of the onion state, so θ is constant if the volume integral is performed only over the domain walls. Hence θ is the angle between the strain and the offset angle. Taking the derivative of U_{total} with respect to θ and setting it to zero, we see that the onion state settles at the energy minimum closest to its initial orientation (the equilibrium offset angle). If strain is small, the resulting torque is roughly proportional to the strain.

Figure 3.3b shows the balance between magnetostatic and magnetostrictive energies, with 200 MPa tension applied at -45 degrees. The magnetostatic energy is lowest at offset angle zero, and the magnetostrictive energy is lowest at 45 degrees (perpendicular to the stress). Total energy is minimized at an intermediate angle of 23 degrees. As we see in Figure 3.3a, this is near the angle that creates maximum torque, so increasing or decreasing strain would be counterproductive.

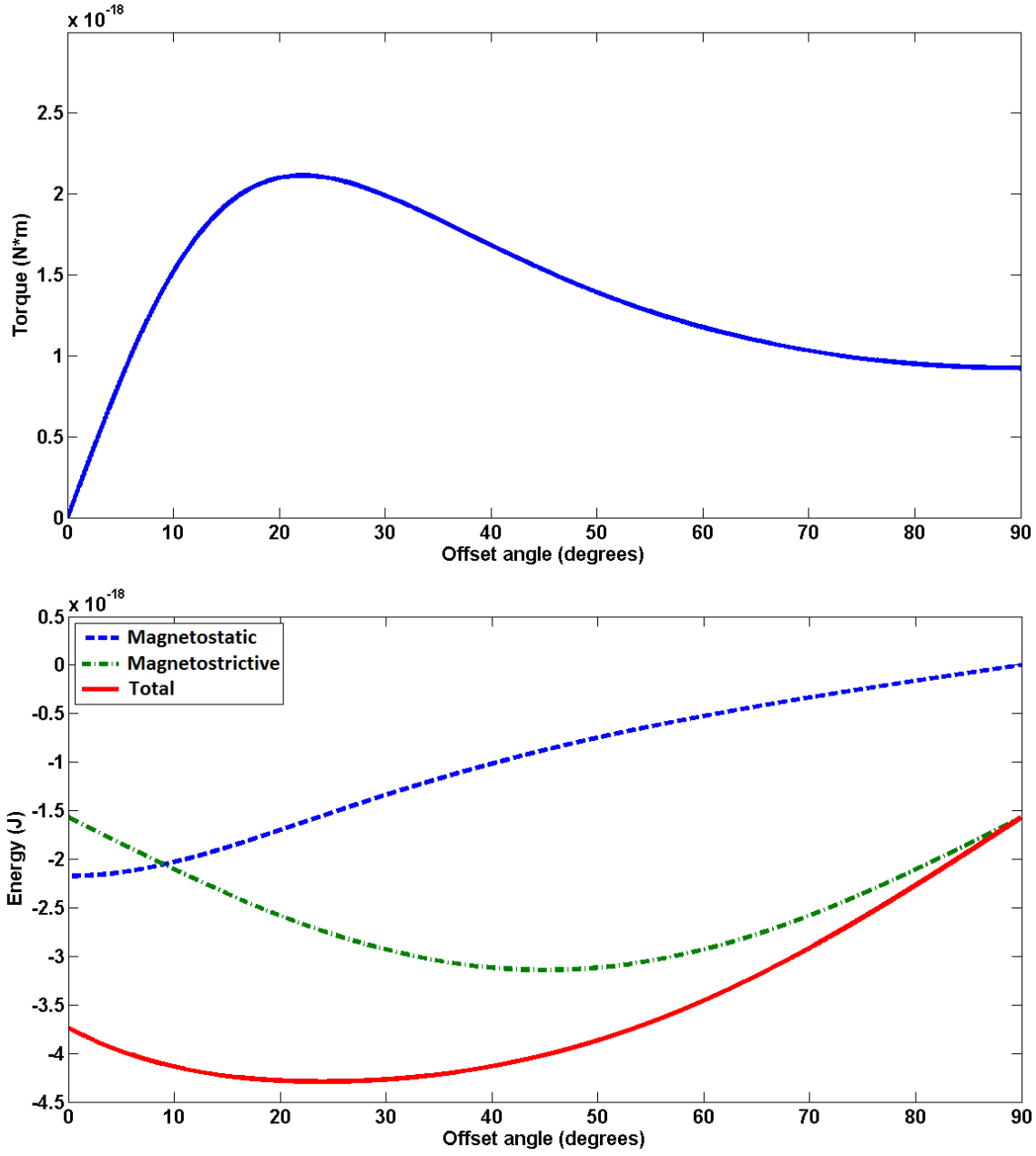

Figure 3.3: a) Variation of torque with offset angle, for actuator described in Table 3.1. b) Magnetostatic and magnetostrictive energies that determine offset angle of the onion state.

If the rotor has a low-friction bearing, torque from the ring will cause it to rotate, shrinking the offset angle and the torque. Simulations using these simplified methods indicate that either stepping motion or continuous rotation is achievable by periodically changing the strain direction in 60-degree increments.

3.2.3 Scaling and Comparison to Electrostatics

Electrostatic actuators are used in MEMS because of the advantageous scaling of electrostatic forces. Madou [27] shows that the maximum force achievable between two electromagnets is proportional to the fourth power of their length (l^4), while electrostatic force between capacitor plates is proportional to l^2. As actuator size decreases, electromagnet force decreases faster than inertia. Electrostatic force decreases more slowly. Force between an electromagnet and a permanent magnet is better, scaling as l^3, but still worse than electrostatics for small sizes. The force between two permanent magnets scales with l^2, like electrostatic force, but is not used for actuation because it cannot normally be controlled.

Multiferroics take advantage of permanent magnet scaling because they do not require current to generate magnetic fields—they use voltage to redirect ferromagnetism. The relative force density of multiferroic and electrostatic actuators does not vary with changes in their size. To compare them, we start by calculating the maximum energy density of the magnetic and electric fields.

Electrostatic field energy density is [27] $U_{es} = \frac{1}{2}\varepsilon_r\varepsilon_0 E_b^2$. For macro-scale gaps in air, the electrical breakdown limit imposes the constraint [27] $E_b \leq 3 \times 10^6$ V/m. By this limit, the maximum electrostatic energy density in air would be ~40 J/m^3, but micro-actuators can be designed to exceed it. For small gaps, or lower than atmospheric pressures, the limit

increases because the breakdown field of air is higher. At sub-micron scales, the breakdown is dominated by field emission rather than ionization, and it becomes strongly dependent on shape but independent of pressure [28]. Since the electric field energy density at small scales is limited by potentially destructive discharges across the gap, reliable devices must maintain a margin of safety below the actual voltage limit. In a device with moving parts, the gap distance varies over time as well as from manufacturing defects. Nonetheless, breakdown voltages as high as 150 V have been demonstrated across a 0.9 micron gap, resulting in a conservative estimation of the electric field at 156 MV/m [28].

The use of dielectric materials also affects the electrical breakdown field. In the piezoelectric ceramics used to apply strain to onion state rings, breakdown field strength of a film is typically around 50×10^6 V/m [29], which implies energy density of about 11,000 J/m^3. Low voltages could therefore be applied across thin piezoelectric films (a few hundred nanometers) and still transfer significant strain energy into a magnetostrictive structure. Higher field strengths are possible in even thinner insulating films, though as they approach the breakdown voltage significant field emission current occurs. [28]. Compared to an air gap in an electrostatic motor, the thickness of a dielectric film is relatively easy to control and does not vary in time, making accidental discharge less likely.

For a magnetic actuator, $U_m = \frac{1}{2}B^2/\mu_0$. The magnetic field B across a gap in a permanent-magnet system cannot exceed the maximum internal field, which is proportional to the saturation magnetization: $B \leq \mu_0 M_s$. In the case of nickel, $M_s = 485$ kA/m, yielding a maximum energy density of 148,000 J/m^3. Although actual magnetic energy density is considerably lower in any real system, the energy density of the electrostatic field in the insulator will still be the limiting factor in the overall force/torque density of a multiferroic

actuator. Unlike an air-gap electrostatic motor, such an actuator could operate independent of pressure, moisture, or the presence of other conductive objects.

3.3 Numerical Simulation and Testing

To validate the predictions in section 3.2, finite element modeling of ring-bar systems was performed in COMSOL Multiphysics, using the weak form LLG equations described in [30] and the methods implemented in [13]. In these LLG simulations the position of the bar is fixed. Table 3.1 gives some key geometric and modeling parameters for the ring-bar system.

Table 3.1: Simulation parameters for numerical calculations.

Property	Outer diam	Inner diam	Bar length	Bar width	Ni thickness	Damping
Value	700 nm	500 nm	350 nm	100 nm	20 nm	0.045

Figure 3.4 shows the result of simulating this geometry, before and after strain is applied.

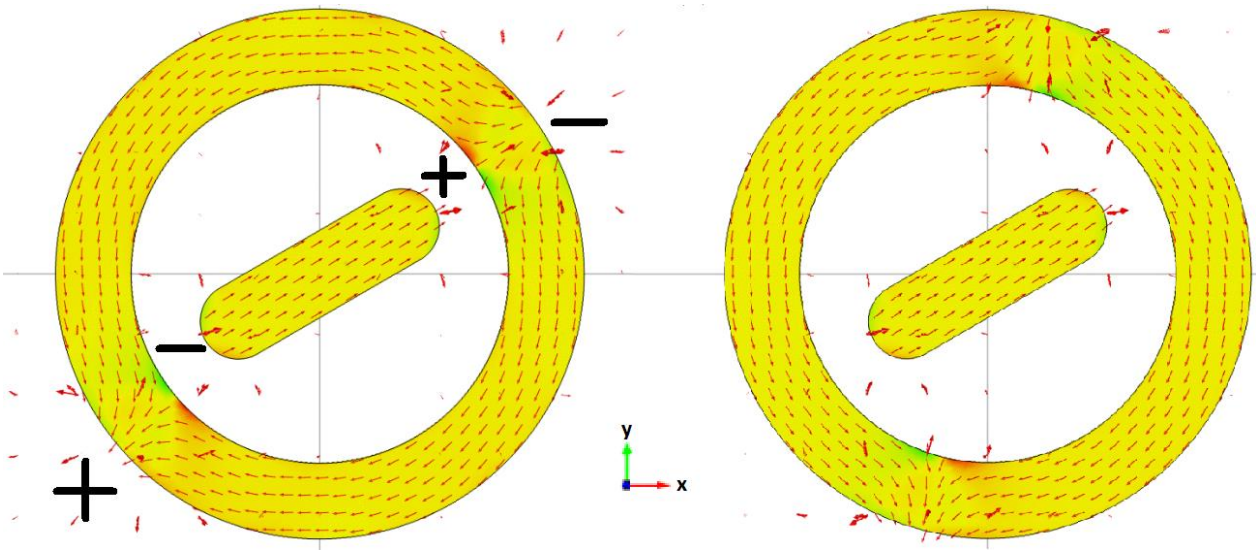

Figure 3.4: Magnetization and stray field in a 700 nm onion-state ring with a bar. Left: at equilibrium after 5 ns. Right: with strain applied to create torque, after 25 ns.

The red arrows inside the ring and bar indicate the direction of magnetization; those outside indicate demagnetizing field, flowing outward from each positive charge and inward toward the adjacent negative charge.

Applying a tensile strain of 200 με in the x direction yields the equilibrium on the right. The onion state rotates away from alignment with the ring (because the magnetostrictive coefficient of nickel is negative) but is not perpendicular because of continued attraction to the poles of the bar.

Torque on each component is calculated as the surface integral of $\boldsymbol{M} \cdot \boldsymbol{H}_{\boldsymbol{demag}}$ [31]. Damping reduced the dipole precession until torques on the ring and bar were equal and opposite, at 2×10^{-18} Nm, consistent with the simplified torque calculation (section 3.2.2). This suggests a torque density of 260 Nm/m^3.

To verify the simulations, we imaged the magnetization of ring-bar systems using X-ray Magnetic Circular Dichroism Photo-Emission Electron Microscopy (XMCD-PEEM), a technique that has been used to characterize the transverse and vortex-type domain walls that can exist in onion-state nano-rings [32], at the Berkeley Advanced Light Source. The sample consists of 30 nm evaporated nickel, initially magnetized in the positive x-direction in figure 3.5 by a 3000 Oe field.

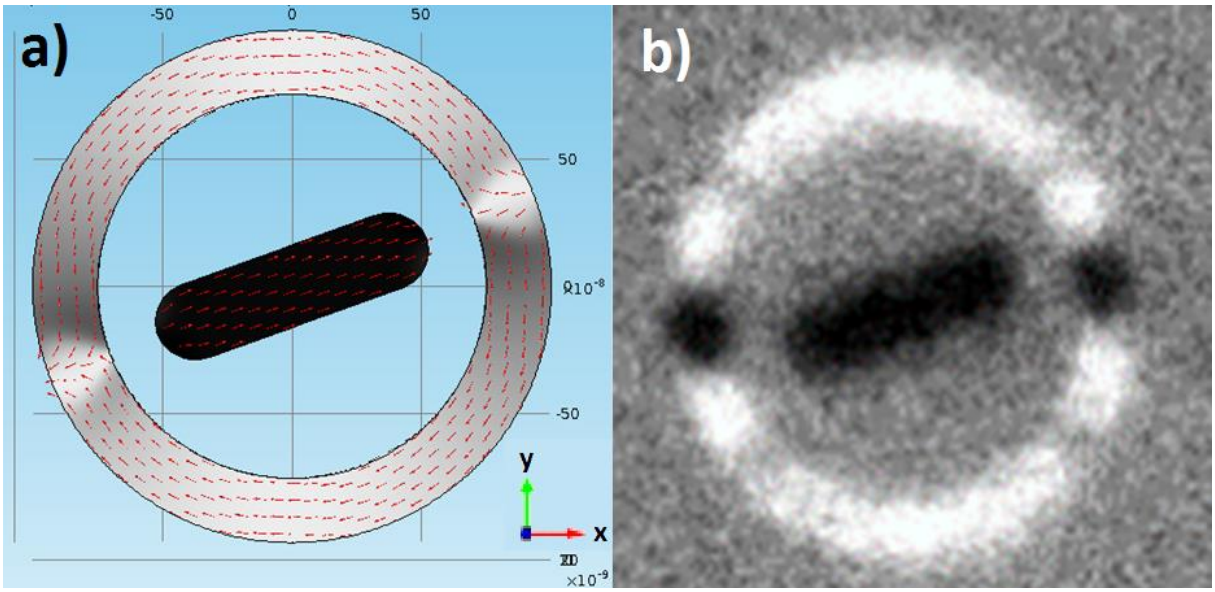

Figure 3.5: a) Simulation results of a nickel ring-rotor system (2-micron ring, 1.6-micron inner diameter, 30 nm thickness), b) PEEM image of an identical 2-micron system.

Figure 3.5 compares one PEEM image with a corresponding finite element prediction. It shows a 2-micron ring with a 1.1-micron bar in the center. In both images, bright areas indicate magnetization to the left and dark areas to the right. Vertical or no magnetization is grey.

This result suggests that the onion state repositioning observed in simulation can occur physically. However, it requires very precise fabrication of the ring, and it proved difficult to reproduce. Even when the geometry of the sample appears correct, most of the samples either form a vortex or multi-domain state instead of an onion state, or the onion state fails to rotate as expected.

Figures 3.6a-e are part of an array of 2-micron and 1-micron rings that did not match the predicted behavior. 3.6a formed an onion state, but it did not rotate because the bar is in a multi-domain state instead of magnetized parallel to its long axis. In 3.6b both onion state

domain walls moved, but in opposite directions—the positive and negative poles of the onion state attract each other as well as repelling the ends of the bar. The ring in 3.6c has collapsed into a vortex state. 3.6d, like 3.6a, formed an onion state that did not rotate. In this case the bar is difficult to see because it is vertically oriented and so its magnetization is vertical (grey).

Figure 3.6e shows a case where the onion state failed to rotate but the bar, overcoming its shape anisotropy, reversed its direction of magnetization; 3.6f is a close-up of a similar case. Although the onion state did not rotate, these support the conclusion that ring-bar systems tend to minimize their magnetostatic energy by aligning the onion state magnetization opposite to the bar magnetization.

Figures 3.6g-i show 1-micron rings from a later sample, this one magnetized initially to the left (white). In 3.6g the onion state has rotated about 130°, not quite far enough to align with the bar. In 3.6h the ring formed a complex multi-domain state. The bar in 3.6i, like e and f, has reversed the direction of its magnetization, but in this case there is also a partial rotation of the onion state (about 45° from its initial horizontal orientation).

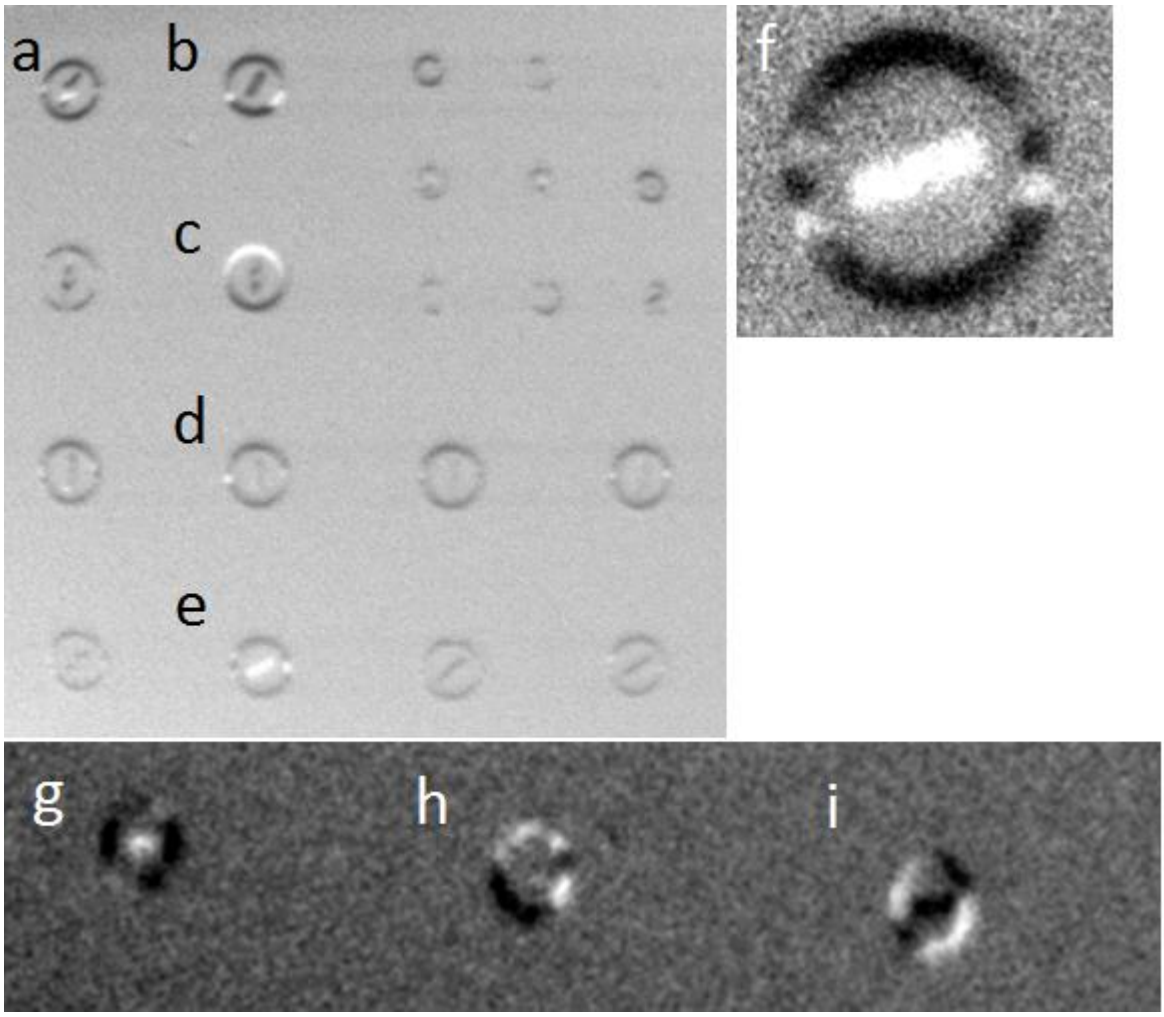

Figure 3.6: PEEM images of unsuccessful and partially successful alignment of onion states with their central bar magnets.

The reasons for these differences from the predicted alignment are not always clear, but some are likely associated with pinning of the onion state domain walls. Pinning might be caused by various factors, including residual strain from the manufacturing process, relatively large crystal boundaries with associated magnetocrystalline anisotropy, or geometric defects such as holes, bumps, or thin points in the ring.

Further experimentation is necessary to understand the factors that make onion rotation successful or unsuccessful, and to confirm that application of strain will produce torque.

3.4 Conclusion

Analysis shows that a bar magnet within an onion-state ring should attract the domain walls, orienting the onion state antiparallel to the bar and pinning the domain walls near the bar ends. This behavior was validated by numerical simulation, and preliminary testing indicated that it can occur in nickel nano-rings, though further experimental analysis is required to characterize the observed behavior.

The prediction that strain can cause a small misalignment of the onion state and thereby create torque was also validated by numerical simulation. Torque predictions using analytical and numerical methods were consistent. Scaling laws show that the torque density of this type of actuator would exceed that of a comparable electrostatic actuator. These results suggest that multiferroic actuators have potential for high torque and power output.

REFERENCES

[1] Kim, K., Xu, X., Guo, J., & Fan, D. L. (2014). Ultrahigh-speed rotating nanoelectromechanical system devices assembled from nanoscale building blocks. Nature communications, 5.

[2] Miyajima, H., Asaoka, N., Isokawa, T., Ogata, M., Aoki, Y., Imai, M., ... & Matsumoto, K. (2003). A MEMS electromagnetic optical scanner for a commercial confocal laser scanning microscope. Microelectromechanical Systems, Journal of, 12(3), 243-251.

[3] Conway, N. J., Traina, Z. J., & Kim, S. G. (2007). A strain amplifying piezoelectric MEMS actuator. Journal of Micromechanics and Microengineering, 17(4), 781.

[4] Syms, R. R. A., Zou, H., Yao, J., Uttamchandani, D., & Stagg, J. (2004). Scalable electrothermal MEMS actuator for optical fibre alignment. Journal of Micromechanics and Microengineering, 14(12), 1633.

[5] Zara, J. M., & Smith, S. W. (2002). Optical scanner using a MEMS actuator. Sensors and Actuators A: Physical, 102(1), 176-184.

[6] Zara, J. M., Bobbio, S. M., Goodwin-Johansson, S., & Smith, S. W. (2000). Intracardiac ultrasound scanner using a micromachine (MEMS) actuator. Ultrasonics, Ferroelectrics, and Frequency Control, IEEE Transactions on, 47(4), 984-993.

[7] Liao, C. D., & Tsai, J. C. (2009). The evolution of MEMS displays. Industrial Electronics, IEEE Transactions on, 56(4), 1057-1065.

[8] Alper, S. E., Azgin, K., & Akin, T. (2007). A high-performance silicon-on-insulator MEMS gyroscope operating at atmospheric pressure. Sensors and Actuators A: Physical, 135(1), 34-42.

[9] Niarchos, D. (2003). Magnetic MEMS: key issues and some applications. Sensors and Actuators A: Physical, 109(1), 166-173.

[10] Bell, D. J., Lu, T. J., Fleck, N. A., & Spearing, S. M. (2005). MEMS actuators and sensors: observations on their performance and selection for purpose. Journal of Micromechanics and Microengineering, 15(7), S153.

[11] Nan, C. W., Bichurin, M. I., Dong, S., Viehland, D., & Srinivasan, G. (2008). Multiferroic magnetoelectric composites: historical perspective, status, and future directions. Journal of Applied Physics, 103(3), 031101.

[12] Hockel, J.L.; Pollard, S.D.; Wetzlar, K.P.; Wu, T.; Zhu, Y.; Carman, G.P., "Electrically controlled reversible and hysteretic magnetic domain evolution in nickel film/Pb(Mg1/3Nb2/3)O3]0.68-[PbTiO3]0.32 (011) heterostructure," Appl. Phys. Lett. , vol.102, no.24, pp.242901,242901-5 (2013).

[13] Sohn, H., Nowakowski, M. E., Liang, C. Y., Hockel, J. L., Wetzlar, K., Keller, S., ... & Candler, R. N. (2015). Electrically-Driven Magnetic Domain Wall Rotation in Multiferroic Heterostructures to Manipulate Suspended On-Chip Magnetic Particles. *ACS nano*.

[14] Rothman, J., Klaui, M., Lopez-Diaz, L., Vaz, C.A.F., Bleloch, A., Bland, J.A.C., Cui, Z. and Speaks, R., "Observation of a Bi-Domain State and Nucleation Free Switching in Mesoscopic Ring Magnets." Phys. Rev. Lett. 86, 1098, 2001.

[15] S. Finizio, M. Foerster, C. A. F. Vaz, C. Mix, M. A. Mawass, A. Tkach, M. Klaui, M. Buzzi, F. Nolting, T. Miyawaki, J. Hockel, G. P. Carman, S. Valencia, and F. Kronast, "Electrical-Field Control of Magnetism Mediated by Strain in Ni Nanostructures Fabricated on pre-poled PMN–PT (011)," Spin, vol. 3 (3), 1340008, (2013)

[16] Hockel, J.L., Deterministic Magnetization Control by Magnetoelastic Anisotropy and its Dependence on Geometry and Scale, Dissertation, UCLA (2013).

[17] Cui, J., Hockel, J.L., Nordeen, P.K., Pisani, D.M., Carman, G.P., and Lynch, C.S., "Giant electric-field-induced magnetic anisotropy reorientation with patterned electrodes on a Ni thin film/lead zirconate titanate heterostructure," J. Appl. Phys. 115, 17C711 (2014).

[18] Hockel, J. L., Bur, A., Wu, T., Wetzlar, K. P., & Carman, G. P. (2012). Electric field induced magnetization rotation in patterned Ni ring/Pb (Mg1/3Nb2/3) O3](1− 0.32)-[PbTiO3] 0.32 heterostructures. Applied Physics Letters, 100(2), 022401.

[19] Hubert, U. & Schafer, R. (2009). *Magnetic Domains: The Analysis of Magnetic Microstructures*. Springer.

[20] Barbic, M., Mock, J.J., Gray, A.P., and Schultz, S., "Electromagnetic micromotor for microfluidics applications," Appl. Phys. Lett. 79, 1399 (2001).

[21] Zhang, L., Abbott, J.J., Dong, L., Kratchovil, B.E., Bell, D., and Nelson, B.J., "Artificial bacterial flagella: Fabrication and magnetic control," Appl. Phys. Lett. 94, 064107 (2009).

[22] Soong, R.K., Bachand, G.D., Neves, H.P., Olkhovets, A.G., Craighead, H.G., and Montemagno, C.D., "Powering an Inorganic Nanodevice with a Biomolecular Motor." Science: 290 (2000) p. 1555-1558.

[23] Fennimore, A. M., T. D. Yuzvinsky, Wei-Qiang Han, M. S. Fuhrer, J. Cumings, and A. Zettl. "Rotational actuators based on carbon nanotubes." *Nature* 424, no. 6947 (2003): 408-410.

[24] Guckel, H., Skrobis, K.J., Christensen, T. R., Klein, J., Han, S., Choi, B., Lovell, E.G., Chapman, T.W. "Fabrication and Testing of the Planar Magnetic Micromotor." J. of Micromechanics and Microengineering, vol. 1, no. 4, 1991, p. 135-138.

[25] Brown, W. F. (1963), Micromagnetics, Interscience Publishers, J. Wiley and Sons, New York.

[26] Lindell, I. (2004). *Differential Forms in Electromagnetics*. IEEE Press.

[27] Madou, M. J. (2009). *Fundamentals of Microfabrication and Nanotechnology, Volume III: From MEMS to Bio-MEMS and Bio-NEMS: Manufacturing Techniques and Applications*. CRC Press, 398-399.

[28] Wallash, A. J. and Levit, L. (2003). Electrical breakdown and ESD phenomena for devices with nanometer-to-micron gaps. Proc. SPIE 4980, Reliability, Testing, and Characterization of MEMS/MOEMS II, 87.

[29] Lebedev, M. and Akedo, J. (2002) What Thickness of the Piezoelectric Layer with High Breakdown Voltage is Required for the Microactuator? Jpn. J. Appl. Phys. 41, 3344.

[30] Szambolics, H., Buda-Prejbeanu, L. D., Toussaint, J. C., & Fruchart, O. (2008). Finite element formalism for micromagnetism. *COMPEL-The international journal for computation and mathematics in electrical and electronic engineering*, *27*(1), 266-276.

[31] Humphries, S. (2012). Surface integral expressions for electric/magnetic force and torque. Field Precision: http://www.fieldp.com/documents/forceandtorque.pdf

[32] A. Locatelli and E. Bauer, "Recent advances in chemical and magnetic imaging of surfaces and interfaces by XPEEM." J. Phys.: Condens. Matter 20 093002 (2008).